JOURNAL OF BIOMOLECULAR STRUCTURE AND DYNAMICS
https://doi.org/10.1080/07391102.2021.1970627

Arjunetin as a promising drug candidate against SARS-CoV-2: molecular dynamics simulation studies

Gandarvakottai Senthilkumar Arumugam[a], Asmita Sen[b], Swati S. Dash[a], Kartik Mitra[c], Mukesh Doble[c], Gopalan Rajaraman[b] and Sathyanarayana N. Gummadi[a]

[a]Department of Biotechnology, Bhupat and Jyoti Mehta School of Biosciences, Applied and Industrial Microbiology Laboratory, Indian Institute of Technology Madras, Chennai, India; [b]Department of Chemistry, Molecular Modelling Group (MMG), Indian Institute of Technology Bombay, Powai, Mumbai, India; [c]Department of Biotechnology, Bhupat and Jyoti Mehta School of Biosciences, Drug Design Laboratory, Indian Institute of Technology Madras, Chennai, India

Communicated by Ramaswamy H. Sarma

ABSTRACT

Stem and bark of the tree *Terminalia arjuna* Wight & Arn. (Combretaceae) has been documented to exhibit therapeutic properties like cardiotonic, anticancer, antiviral, antibacterial, antifungal, hypercholesterolemia, hypolipidemic, and anti-coagulant. Our previous studies have shown that, ethanolic extract of *T. arjuna* bark exhibits radical scavenging anti-oxidant activity and also effectively inhibited catalase activity. In this study, oleanane triterpenoids type compounds *viz.,* oleanolic acid, arjunolic acid, arjunolitin, arjunetin were isolated from ethanolic bark extract as bio-active compound and their structures were elucidated using ^{1}H, ^{13}C NMR, HR-ESIMS, IR. Of the various compounds, Arjunetin showed significant inhibition of catalase activity as compared to the other compounds. Based on the structural similarity between arjunetin and current antiviral drugs, we propose that arjunetin might exhibit antiviral activity. Molecular docking and molecular dynamics studies showed that arjunetin binds to the binds to key targets of SARS-CoV-2 namely, 3CLpro, PLpro, and RdRp) with a higher binding energy values (3CLpro, −8.4 kcal/mol; PLpro, −7.6 kcal/mol and RdRp, −8.1 kcal/mol) as compared with FDA approved protease inhibitor drugs to Lopinavir (3CLpro, −7.2 kcal/mole and PLpro −7.7 kcal/mole) and Remdesivir (RdRp −7.6 kcal/mole). To further investigate this, we performed 200–500 ns molecular dynamics simulation studies. The results transpired that the binding affinity of Arjunetin is higher than Remdesivir in the RNA binding cavity of RdRp. Based on structural similarity between arjunetin and Saikosaponin (a known antiviral agents) and based on our molecular docking and molecular dynamic simulation studies, we propose that arjunetin can be a promising drug candidate against Covid-19.

ARTICLE HISTORY
Received 25 May 2021
Accepted 16 August 2021

KEYWORDS
Terminalia arjuna; catalase inhibition; SARS-CoV-2 protease; arjunetin; molecular docking; molecular dynamic simulations

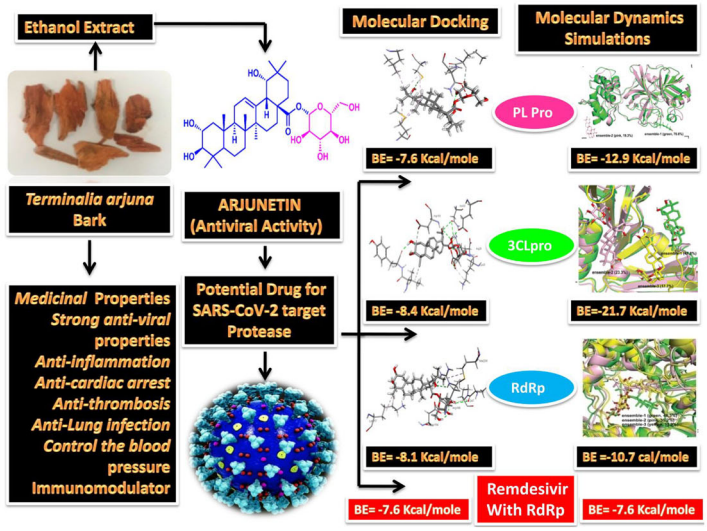

Abbreviations: 3CLpro: protease 3C-like preotease; PLpro: papin like protease; RdRP: RNA dependent RNA polymerase; DPPH: 2,2-Diphenyl-1-picryl hydrazyl radical; RMSD: root-mean-square deviation

CONTACT Sathyanarayana N. Gummadi gummadi@iitm.ac.in Department of Biotechnology, Bhupat and Jyoti Mehta School of Biosciences, Applied and Industrial Microbiology Laboratory, Indian Institute of Technology Madras, Chennai, 600 036, India; Rajaraman Gopalan rajaraman@chem.iitb.ac.in Department of Chemistry, Molecular Modelling Group (MMG), Indian Institute of Technology Bombay, Powai, Mumbai 400076, India.

Supplemental data for this article can be accessed online at https://doi.org/10.1080/07391102.2021.1970627

1. Introduction

The World Health Organization reported that infectious diseases caused by pathogenic microorganisms to account for about 25% of the total annual deaths that occur worldwide, both in developed as well as developing countries; with the incidence being higher in developing nations (WHO, 2012). In the present time, drastic changes in climate and increasing levels of pollutants in the atmosphere result in accelerating the rate of genetic mutations in these microorganisms, thereby increasing their infectivity. Climate change also increases the contact of insect vectors and animal reservoirs of pathogens with humans, resulting in the emergence of new diseases which are unresponsive to available treatment regimes. Overuse of antibiotics also leads to the emergence of multi-drug resistant strains that are hard to eliminate. Therefore, the discovery of new and novel antibacterial and antivirals coupled with a better understanding of the mechanism of action is the present challenge in research.

The FDA approved COVID-19 drugs including Remdesivir and Lopinar suffers a major challenge of post treatment side-effects. For example, remdesivir is a potent drug against SARs-CoV-2, however continuous treatment with remdesivir was found to exert cardiotoxicity which leads to post-treatment complications (Seong et al., 2020; Yu et al., 2021). Recent clinical analysis of 1375 case reports has shown that 8.4% of patients treated with remdesivir has suffered serious cardiac complication with a mean cardiac event time as 3.3 days (Concetta et al., 2021).

In this aspect, plant-derived phytochemicals can offer a new direction in developing methods for disease control. The major advantage of these traditional systems of medicine such as Ayurveda, Siddha, or Unani is that, they depend on natively available flora and has been in treatment of almost all kinds of maladies for centuries. Recent studies have also shown natural products have potential alternate therapeutics against SARs-CoV-2 (Cheorl, 2021). For instance Rotiorinol-C and Scutifoliamide-A has shown potent binding towards SARs-CoV-2 RDRp (Sinosh et al., 2021). Glycyrrhizin, a bio-active triterpenoid phytochemical from *Glycyrrhiza glabra* has potent inhibitory effect against SARs-CoV-2 protease and replicase protein (Lukas et al., 2021). Further, the antioxidant and anti-inflammatory property of Glycyrrhizin was also found to exert protection against the organ damage thereby improving the therapeutic outcome (Zhaoyan et al., 2021). Similarly, Saikosaponin, a triterpenoid from Bupleuri Radix, has shown potent inhibitory activity against SARs-CoV-2 proteases and RdRp (Xian et al., 2020). There is a strong need in isolating novel antiviral molecules from traditional medicinal plants, with minimal side effects.

Terminalia Arjuna (TA) (Family: Combretaceae), a tree native to the Indian subcontinent, is extensively used in many traditional forms of medicine for the treatment of hypertension and coronary heart diseases (Dwivedi & Chopra, 2014), earning it the epitaph of 'Guardian of the heart'. It is known to confer cardioprotective properties such as strengthening heart muscles and improving the functioning of cardiac muscles, thereby alleviating heart failure, angina and hypercholesterolemia. Stem and bark of this plant exhibit various other therapeutic properties such as expectorant, anti-dysenteric, purgative, laxative and have also been used to treat leucoderma, anemia, hyperhidrosis, asthma, and tumors (Jain et al., 2009). In addition, it has also been reported that the bark of *T. arjuna* also possesses good anticancer, antiviral, and antimicrobial activities (Cooper, 2005; Patil & Gaikwad, 2011; Tripathi & Singh, 1996). It has been hypothesized that the cardioprotective activity of TA bark extracts is likely by the activation of endogenous antioxidant molecules by triterpenes, namely arjunolic acid (Dwivedi, 2007; Pawar & Bhutani, 2005; Sumitra et al., 2001).

Previous studies carried on the elucidation of properties of *T. arjuna* showed that catalase activity was inhibited by ethanolic bark extract *in vitro* (Padma Sree et al., 2007). The enzyme catalase is one of the endogenous antioxidant defense systems that help in decreasing the accumulation of reactive oxygen by decomposing hydrogen peroxide during cellular metabolism to water and molecular oxygen. It is postulated that catalase activity protects pathogens from inactivation by reactive oxygen species (ROS) in eukaryotic systems, making it a potential virulence factor in many bacterial pathogens. Studies have shown that catalase facilitates intracellular survival of bacterial pathogens such as *Mycobacterium tuberculosis* (Manca et al., 1999), *Campylobacter jejuni* (Day et al., 2000), *Helicobacter pylori* (Basu et al., 2004**),** and Herpes Simplex Virus (Newcomb et al., 2012). It has also been reported that increased serum catalase activity may also alter immune function, viral replication, and/or repair processes (Roth et al., 1987; Schreck et al., 1991**)**. In this regard, the catalase inhibitor in *T. arjuna* extract necessitates further research.

We believe *T. arjuna* stands as a potential candidate for the development of an effective therapeutic agent for the current pandemic respiratory disease, COVID-19, which emerged in December 2019 and has been spreading at a rapid rate all over the world with a high rate of infectivity and mortality. The viral pathogen, SARS-CoV-2, appears to spread more efficiently, making it difficult to contain and increasing its pandemic potential (Wu et al., 2020; Situation report 15 May 2020). One of the important pathological aspects of COVID 19 is its effect on the cardiovascular system and *T. arjuna* has well-documented cardioprotective properties, making it an excellent match. Catalase inhibition is another important aspect that has been shown to inhibit viral replication and spread. Literature shows that bark extract of *T. arjuna* possesses anti-herpesvirus activity in preventing viral attachment and penetration and also disturbing the late event of infection (Hua et al., 2002).

Consolidating information available from literature and experiments conducted in our lab on *T. arjuna* extracts, it is evident that *T. arjuna* can be regarded as an apt candidate in the search for antivirals against COVID-19. In this study, different solvent extracts of TA and the purified compounds from ethanol extracts have been evaluated for their effect on catalase activity. Also, molecular docking studies of the isolated compound from ethanolic bark extract have been carried out on protease of SARS-CoV-2. To further confirm

this, we performed molecular dynamics simulation studies and found that arjunetin is a potential inhibitor against three proteases of SARS-CoV-2 viz. 3CLpro, PLpro, and RdRP as compared with FDA approved drugs Lopinavir and Remdesivir. The present study will serve as a frontier for the much-needed research on drug development for COVID-19.

2. Materials and methods

2.1. Collection of plant materials

The dry stem bark of *Terminalia arjuna* was obtained from the Centre of Traditional Medicine and Research (CTMR), Chennai, India, and collected from Pillaiyarpattai, Sri Karpagam Vinayager Temple thalaviruksha, Sivagangai District, Tamil Nadu, India, and authenticated at Siddha Central Research Institute, Arumbakkam, Chennai, Tamil Nadu, India (voucher specimen no.: T19081901A).

2.1.1. Chemicals and reagents

Bovine serum catalase (CAS Number. 9001-05-2) and DPPH (2,2-Diphenyl-1-picryl hydrazyl radical) CAS Number 1898-66-4 was obtained from Sigma Aldrich, USA. Silica gel (230–400 mesh) and Sephadex LH-20 column obtained from Merck India and GE Healthcare, India, respectfully. All the solvents used for extraction were AR grade procured in India. Ethanol (95% v/v technical grade) was purchased from Hayman, India.

2.1.2. Preparation of the crude extract

Air-dried and finely powdered *T. arjuna* bark (75 g) was extracted using Soxhlet apparatus with various solvents for 72 h using sequential refluxing with solvents of increasing polarity hexane (100 mg), chloroform (400 mg), ethyl acetate (240 mg), acetone (3 g), ethanol (12 g) and water (3 g). After filtration and evaporation of solvents under a vacuum, the residues were stored at room temperature. Phytochemical tests were carried out to detect the presence of tannins, alkaloids, reducing sugars, saponins, flavonoids (Padma Sree et al., 2007)

2.2. Extraction and isolation of compounds from T. arjuna bark

1.5 kg of air-dried bark of TA was ground to a fine powder and sequentially extracted with solvents of increasing polarity (hexane, chloroform, and ethanol each solvent 5 L) for 72 h using Soxhlet apparatus. After filtration, evaporation was done under a vacuum, and the residues were stored at room temperature. A glass column (60 cm × 50 mm) packed with silica gel (60–120 mesh) was used as a stationary phase for the separation of phytochemicals in solvent extracts. Hexane fraction (10 g) was eluted by column chromatography over silica gel (60–120 mesh) using a varying concentration of chloroform in hexane as eluent (0–100% chloroform) to afford two fractions, one at hexane-chloroform (9:1) to yield the mixture of compounds and at (1:1) to yield compound **1** (50 mg). Chloroform fraction (55 g) was subjected to chromatography on silica geleluting with hexane-EtOAc-methanol gradient to afford five fractions A-E. Fraction C (4:1, ethylacetate:hexane) was further purified by preparative TLC using $CHCl_3$ as a solvent to yield compound **2,** which was pale yellow in color (500 mg). Fraction D (4:1, ethylacetate:methanol) was purified to obtain compound **3** as a pale yellow color powder (50 mg). Ethanol fraction (4 g) was column chromatographed over Sephadex LH 20 using various concentrations of methanol and water as eluent at 100% methanol to afford compound **4** as white crystalline solid (10 mg). The detailed scheme is given in supplementary material (Figure S6).

2.3. Analytical techniques

UV spectra were recorded on a Jasco V 550 UV-VIS spectrophotometer. IR spectra were recorded on a Perkin Elmer spectrum one Fourier Transform Infrared spectrometer with KBr pellets. ^{1}H and ^{13}C NMR spectra of compounds were recorded on a JEOL 400 MHz NMR spectrometer in $CDCl_3$ with TMS as internal standard and with chemical shifts (δ) reported in ppm. HRESIMS were measured on a Q-TOF micro mass spectrometer (Waters USA) in positive ion mode with methanol as solvent. The operating parameters of the Varian E112 EPR spectroscopy instrument were as follows: Frequency: 9.23 Hz, Microwave Power: 10 mW, Mod. Constant: 3.2, G-Time Constant: 0.5, Center Field: 3300, G-Scan range: 2000. All scans and sample positions were carried out with the same conditions.

2.4. Free radical scavenging assay using UV-visible spectroscopy

The antioxidant capacities of *T. arjuna* extracts were evaluated by measuring their free radical abilities to1,1-diphenyl-2-picryl hydrazyl (DPPH) stable radicals following established procedure by measuring the absorbance of 3 ml of 100 mM DPPH (ethanolic solution) that contained 20 µl of extract (1 mg/ml each extract). Ethanolic solution of 100 mM DPPH was taken as the blank (Moure et al., 2001). The disappearance of DPPH color was measured spectrophotometrically at 517 nm (Jasco V 550 UV-VIS, Tokyo, Japan). Inhibition of free radical DPPH in percent (%) by the following formula

$$\text{Inhibition } (\%) = 100 \times \left(\frac{A_{blank} - A_{sample}}{A_{blank}}\right)$$

where A_{blank} is the absorbance of DPPH solution without extract, and A_{sample} is the absorbance of the tested extract.

2.5. Free radical scavenging assay using EPR spectroscopy

EPR spectroscopy was used to monitor the scavenging of DPPH radicals by the TA extracts. 20 µl of TA extracts were mixed with 100 µl of methanolic solution of DPPH to a total volume of 3 ml, and the EPR spectrum was measured using VARIAN E-112 ESR spectrometer at different time

points. 3 ml of 100 mM DPPH in ethanol was taken as blank. The decrease in the intensity of the DPPH peak, which was indicative of a decrease in the concentration of DPPH radical, was monitored by an EPR spectrometer for a period of 30 min during which the radical was stable (Adevaiton et al., 2009). The DPPH radical was generated in ethanol solution and considered as a control (Figure S5). The DPPH radical scavenging activity was estimated as a ratio of individual DPPH signal peak height to that of control.

2.5.1. DPPH radical scavenging activity

$$1-(Aofsample)\Big/_{(Aofcontrol)}$$

The DPPH radical scavenging activity of each sample was calculated by comparison of relative peak height for control (sample free) DPPH solution. DPPH radical reducing activity of each test sample was expressed as the percentage of DPPH residue

2.6. Catalase assay

The assay mixture contained 10 μg of extracts, 63 μl of 0.132 M hydrogen peroxide, 70 μl of 0.002 mg/ml catalase, and the volume was made up to 700 μl with 50mMphosphate buffer at pH 7.0. Assay with an equal volume of corresponding solvent instead of extracts was used as blank. Similarly, a catalase assay was performed withcompound**4** from ethanol extract with increasing concentrations within the range of 10 μg–50 μg with the same conditions as described above. All the experiments were performed at least three times and the values mentioned are mean values within ± 5% standard error. One unit of catalase activity is defined as the amount of enzyme required to break one micromole of substrate per minute.

2.7. Molecular docking studies

The structures of the respective targets have been retrieved from PDB and have been prepared for docking using UCSF Chimera Dock Prep Module and AutoDockVina (Oleg et al., 2010). The targets 3CL Pro (PDB-6lu7), PL-Pro, and RNA-polymerase (PDB:6M71) were prepared for docking by adding hydrogen, assigning charges, and removing water molecules using the dock prep module (Kartik et al., 2020). For 3CL-Pro, grid box of size 27*27*27 centered at coordinates (−16.1115, 12.1099, 66.6681) was made, and docking was performed, and for PL-Pro grid box of size 29*29*29 centered at coordinates (−1.84143, 0.0274012, 1.57883) was made and docking was performed. In the case of RNA polymerase, the grid box of 35*29*30 centered at coordinates (−1.84143, 0.0274012, 1.57883). The pose with the lowest binding energy was considered as the best pose and saved for further study.

2.8. Molecular dynamics and simulation studies

The molecular dynamics simulations have carried out using the protein-inhibitor complexes, namely, 3CL-protease (PDB entry 6lu7) and PL-protease (PDB entry 6w9c) complexed with both arjunetin and Lopinavir and also RNA-polymerase (PDB:6M71) complexed with arjunetin and Remdesivir, with the starting structures obtained from the molecular docking studies. The RESP charges (Bayly et al., 1993; Fox & Kollman, 1998) of the small molecule (inhibitor) have been calculated in the HF/6-31G* level using the Gaussian 09 program (Frisch et al., 2009) Generalised amber force field (gaff2) (Wang et al., 2004) and ff14SB force field (Maier et al., 2015) were used for the ligand and protein, respectively. Sodium ions were added to neutralize the system. The neutralized system was then solvated with the TIP3P water molecules (Mark & Nilsson, 2001), extending to 10 Å in a cubic box. The solvated system is then energetically minimized to remove the atomic clashes using the SANDER module implemented in Amber16 (Case et al., 2005, Case et al., 2008; Pearlman et al., 1995; Salomon-Ferrer et al., 2013a). The minimization has been carried out in two successive stages. The system is minimized for 5000 steepest descent steps (Petrova & Solov'ev, 1997) followed by 10,000 steps of conjugate gradient method (Shewchuk, 1994). After successfully minimizing the system, the next stage is to allow the system to slowly heat from 0.1 K to 300 K over 50 ps in a constant volume. During the heating process, the ligand molecule was restricted with the positional restraints of 10 kcal/mol Å^2. The restraints were slowly removed over the 7-stages of equilibration, reducing the restrictions as 10, 8, 6, 4, 3, 2, 1, 0.5 kcal/mol Å^2, with each equilibration for 30 ps (Ghodke et al., 2019; Priyadarshinee et al., 2016). These short equilibration steps were carried out using constant pressure periodic boundary conditions (isothermal–isobaric ensemble, NTP). The pressure was maintained to 1 atm using weak-coupling Berendsen barostat with a pressure relaxation time of 1 ps (Dickson et al., 2014). Each equilibration is followed by minimization using the same protocol used in the initial minimization step (5000 steps of steepest descent followed by 10,000 steps of the conjugate gradient). These minimized systems were used as the starting structure for the next equilibrations. After all 7-steps of equilibration, a 50 ps equilibration was performed without any restrain before the final production run. Finally, a 200 ns long unrestrained production (100 ns for the RNA-polymerase-Remdesivir system) has run under NTP condition using periodic boundary condition for each protein-ligand complex using GPU accelerated version of Particle Mesh Ewald Molecular Dynamics (PMEMD) method implemented in Amber 16 (Salomon-Ferrer et al., 2013a). During the simulation, the pressure is kept fixed at 1 atm using Berendsen barostat, with the pressure relaxation time of 1 ps. The temperature of the system is fixed at ∼300 K using Langevin Thermostat (Larini et al., 2007). All bonds involving hydrogens are constrained during the final production using the SHAKE algorithm (Andersen, 1983) with an integration time step of 2 fs. A cut-off value of 10 Å has been used for the nonbonded interactions (van der Waals as well as electrostatic interactions) by Particle Mesh Ewald

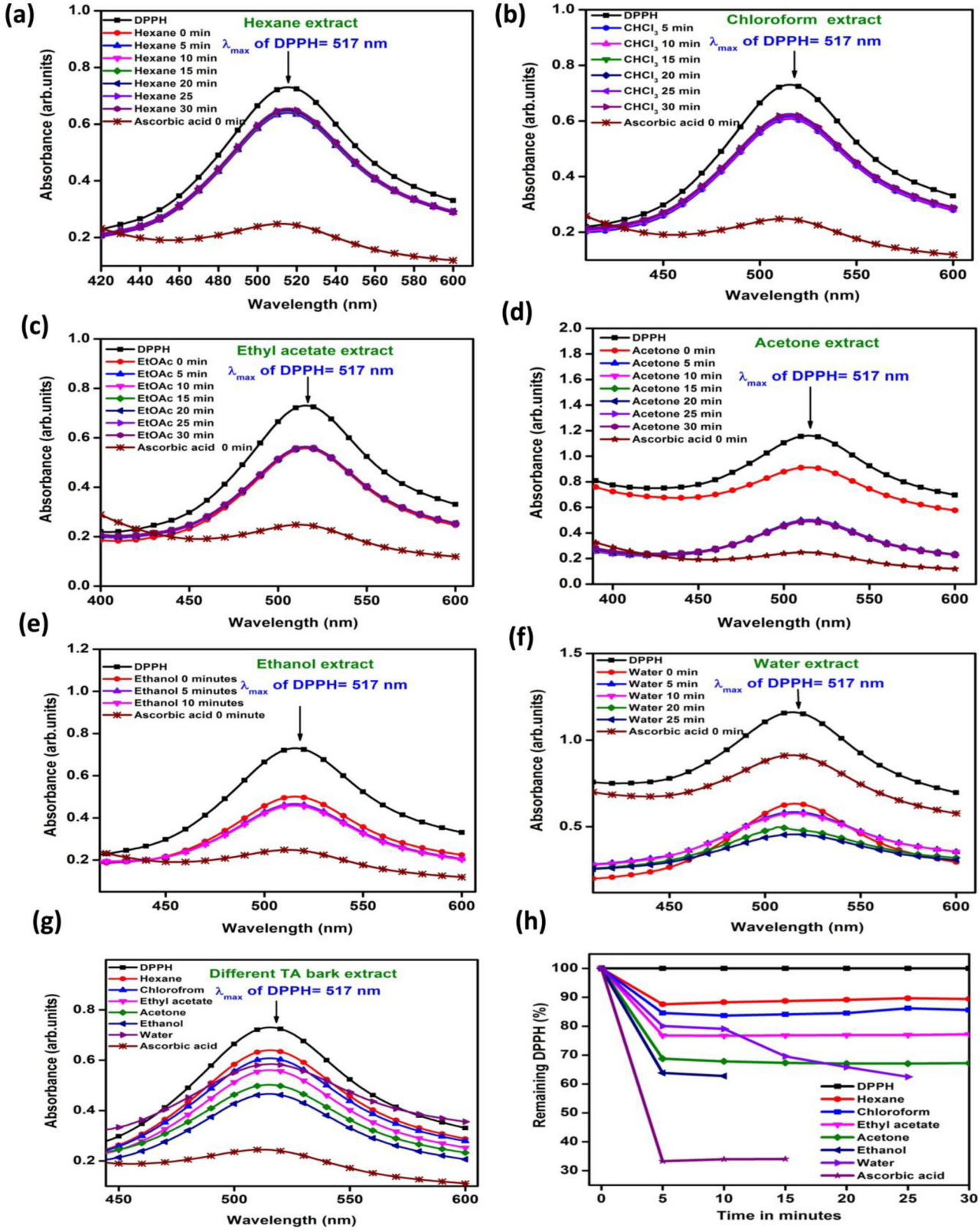

Figure 1. DPPH radical scavenging activity with different extracts by UV/vis (a) Hexane, (b) Chloroform, (c) Ethyl acetate, (d) Acetone, (e) Ethanol, (f) Water, (g) Comparison of DPPH radical scavenging activity with different TA bark extract with DPPH and with standard (ascorbic acid) by UV/visible, (h) Comparison % inhibition for different TA bark extract with DPPH and with standard (ascorbic acid) by UV/vis spectrum.

(PME) method (Salomon-Ferrer et al., 2013b; Darden et al., 1993, 1999). The coordinates were saved at every 2 ps, and a total of 100,000 frames were recorded for 200 ns of simulations.

Cluster analysis, RMSD values, the hydrogen-bond analysis were performed using the CPPTRAJ module (Roe & Cheatham, 2013) of AMBER16 for every frame over 200 ns of the production run. The binding energies of ligands

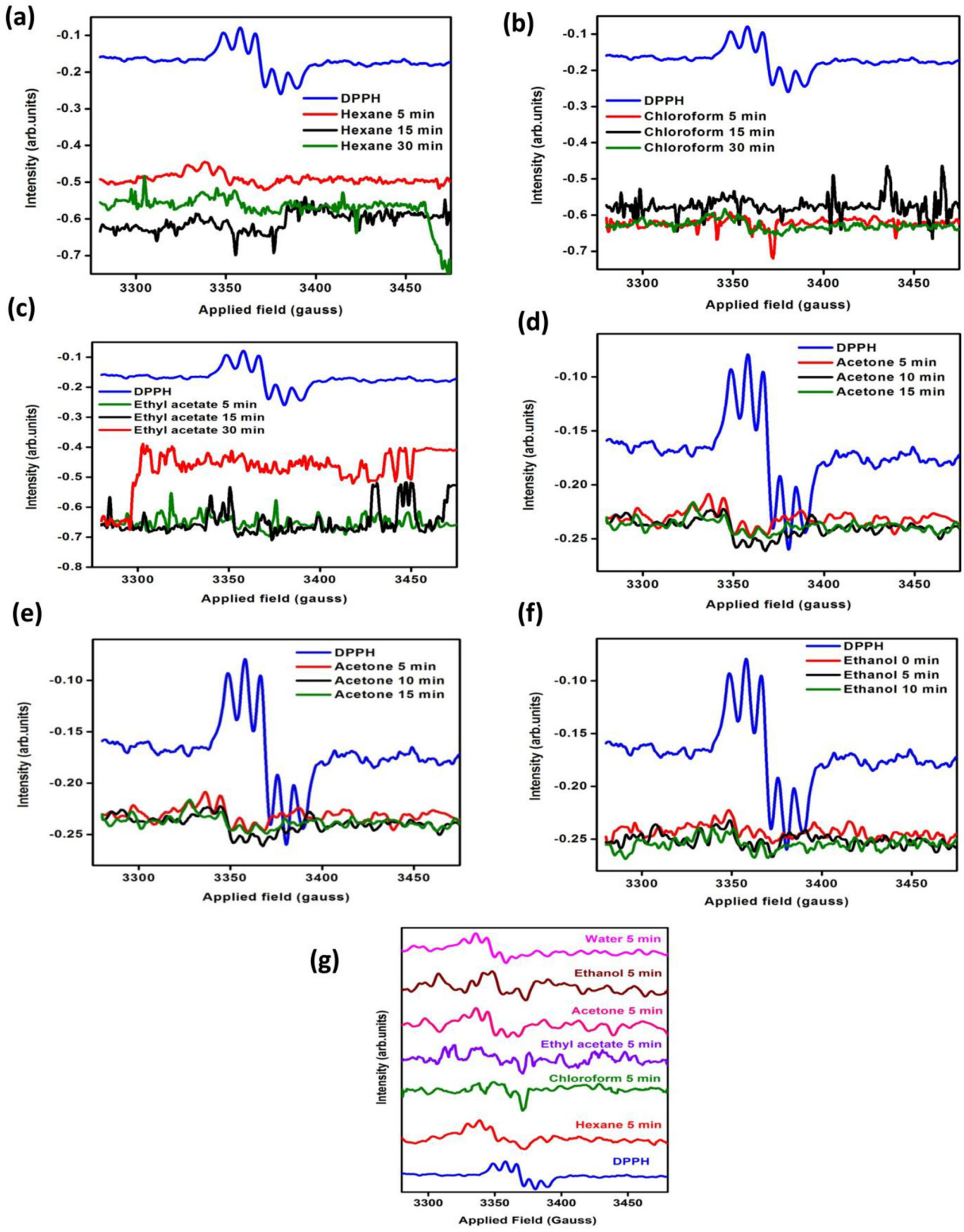

Figure 2. EPR spectra of DPPH with various extract (a) Hexane extract, (b) Chloroform extract, (c) Ethyl acetate extract, (d) Acetone extract, (e) Ethanol extract, (f) Water extract, (g) Comparison of the EPR spectra of DPPH and different TA extract with DPPH at 5 min.

were estimated using the MM-PB/GBSA method using the MMPBSA. py program (Miller et al., 2012) in the Amber Tools package, considering a total of 1000 steps at different stages during the simulation considering each frame. The UCSF Chimera (Pettersen et al., 2004) was used for visualizing the MD trajectories, and PyMOL 2.4.1 (http://www.pymol.org) was used for preparing images (DeLano, 2002).

3. Results and discussion

3.1. 2, 2-diphenyl-1-picrylhydrazyl (DPPH) free radical scavenging assay

Scavenging of DPPH radicals, which have maximum absorption at 519 nm in ethanol by antioxidants, results in a decrease in absorption over time which can be monitored using a UV-visible spectrophotometer at room temperature. Scavenging capacity can be represented as % inhibition of DPPH radical. In this study, a marked decline of the absorption intensity at 517 nm was observed after adding 10 µl of *T. arjuna* bark extracted in various solvents (hexane, chloroform, ethyl acetate, acetone, ethanol, and water molecule) individually to DPPH solution. The results from different bark extracts were compared with those from ascorbic acid, a known antioxidant, at various time intervals (Figure 1a–f). The decrease in absorption could be attributed to the phytochemicals in the bark extracts, which donate protons to DPPH and decolorize it (Figure S1). It was found that the extracts varied significantly in terms of antioxidant activity. Percentage inhibition of DPPH radical scavenging activity at 5 min followed the order ethanol (36.18%) > acetone (31.24%) > ethyl acetate (23.75%) > water (19.93%) > chloroform (16.79%) > hexane (12.41%). Ethanolic extract showed the highest activity (36.18%) compared with other extracts, which was equivalent to ascorbic acid, the standard antioxidant (66.72%) (Figure 1g and 1h).

EPR spectroscopy was used to quantify the rate of DPPH radical disappearance in the presence of bark extract in this study. This technique has been used previously to assess the free radicals scavenging ability of compounds (Justyna et al., 2013; Ningijian & David, 2014). EPR determination of antioxidant activity is based on measuring the changes in the intensity of the EPR spectrum of stable radicals that result from their interaction with bark extracts antioxidants. In this study, the EPR spectrum of ethanolic solutions of DPPH with various extracts was compared to the spectrum obtained from pure DPPH in order to study the decline in DPPH signal intensity (Figure S2), which indicated scavenging. Ethanolic solutions of DPPH were mixed with solutions of prepared bark extract, and a decline in DPPH signal intensity was monitored by EPR (Figure 2a–f). Antioxidant activity (AA) of different extracts was measured based on remaining DPPH residue (%), and it was in the order of hexane (77.10%) > chloroform (76.25%) ethyl acetate (74.95%) > acetone (70.69%) > ethanol (68.10%) > water (65.23%) at 5 min. Based on the above results, antioxidant activity trends were observed in the order of water- > ethanol > acetone > ethyl acetate > chloroform > hexane, the decrease in DPPH peak intensity observed to be highest in water and ethanol extract (Figure 2g), indicating their superior antioxidant property as compared to extracts in other solvents, which is in correlation with previous studies (Orhan et al., 2007; Zivkovic et al., 2009).

3.2. Isolation and structure elucidation

Four different compounds were isolated from TA extracts and were identified using IR spectrum studies, ^{13}C NMR, and ^{1}H NMR. Compounds 1, 2, and 3 were identified as oleanolic acid, arjunolic acid and arjunolitin. Details of all spectrophotometric data have been provided in the supplement section (Figures S3–S5).

Compound 4 was obtained as colorless solid from ethanol fraction using 100% methanol as eluent. It showed UV λ_{max} (methanol) at 423 nm. It exhibited characteristic IR absorption bands trisubstituted double bonds (1630 cm^{-1}, 894 cm^{-1}), hydroxyl (3355 cm^{-1}), ester (1730 cm$^{-1)}$, methyl (1452 cm^{-1}), gem dimethyl 1391 cm^{-1}, C-O stretching frequency (1260, 1161, 1049 cm^{-1}). On the basis of mass and ^{13}C NMR spectra the molecular ion peak of 4 was determined at *m/z*673.4 $[M+Na]^+$ $C_{36}H_{58}NaO_{10}$, *m/z* 689 $[M+K]^+$, *m/z* 511 $[M\text{-}162]^+$, *m/z* 527 $[M\text{-}162\text{-}44]^+$, *m/z*430 $[M\text{-}162\text{-}44\text{-}34]^+$, *m/z* 413 $[M\text{-}162\text{-}44\text{-}41]^+$supported one glycoside, three removable hydroxyl group and one ester function in the molecule (Figure S5).

^{1}H NMR spectrum of compound (4) exhibited signals of an olefinic proton at δ_H 7.0 (1H, brs, H-12) and seven methyl singlet's δ_H (0.12, 0.16, 0.19, 0.33, 0.36, 0.40, 0.57, 7XCH_3, 21H), the spectrum showed three oxygen bearing methine protons at δ_H 4.47 (1H, brs, H-19), δ_H 4.66 (1H, s, H-3α), δ_H 4.73 (1H, d, $J = 9.5$ Hz, H-2β), δ_H 3.48 (1H, brs-H18), δ_H 3.32–3.89 (glucose hydrogen's). ^{13}C NMR spectrum displayed 36 signals inclusive of seven methyl signals δ_C (13.9, 16.9, 17.0, 17.6, 23.5, 25.8, and 27.3), three secondary hydroxyl groups δ_C 69.7 (C-2), 75.6 (C-3), 77.9 (C-19), one trisubstituted double bond δ_C 121.8 (C-12), 144.2 (C-13), ester carbonyl δ_C 175.4 (C-28), glucose carbon δ_C 60.2, 60.8, 67.6, 72.5, 76.8, 94.26. The anomeric proton signals at δ_H 6.8 (1H, -H1′) in the ^{1}H NMR spectrum and anomeric carbon signals at δ_H 94.2 in the ^{13}C NMR spectra of compound attributed to a β-glucose unit linked to the C_{28} carbonyl group of the genin through an ester bond (Honda et al., 1976; Sunyana et al., 2009; Tripathi & Singh, 1996). From the above, all spectroscopic data the compound 4 was named arjunetin.

Previous results showed that ethanolic extract had significantly higher antioxidant ability compared to extracts from other solvents. Since arjunetin is the identified phytochemical in the ethanol fraction, it may have higher therapeutic significance as compared to other compounds isolated and identified. This is further confirmed in our studies on catalase inhibition, as described in the next section.

3.3. Catalase assay with arjunetin (Compound4) from ethanol extract of TA bark

Different bark extracts of *T. arjuna* showed inhibition of catalase activity. Amongst all the extracts least inhibition was noted with chloroform extract, and maximum inhibition was observed with ethanol extract (Figure 3a and 3b). Dose-dependent studies of isolated arjunetin molecule from ethanolic bark extract on catalase activity showed that inhibitory effect increased with increasing concentration of arjunetin (Figure 3c snd 3d). This is in contrast with previous findings where it has been observed that ethanolic bark extracts enhanced the catalase levels *in vivo* in the ischemic heart

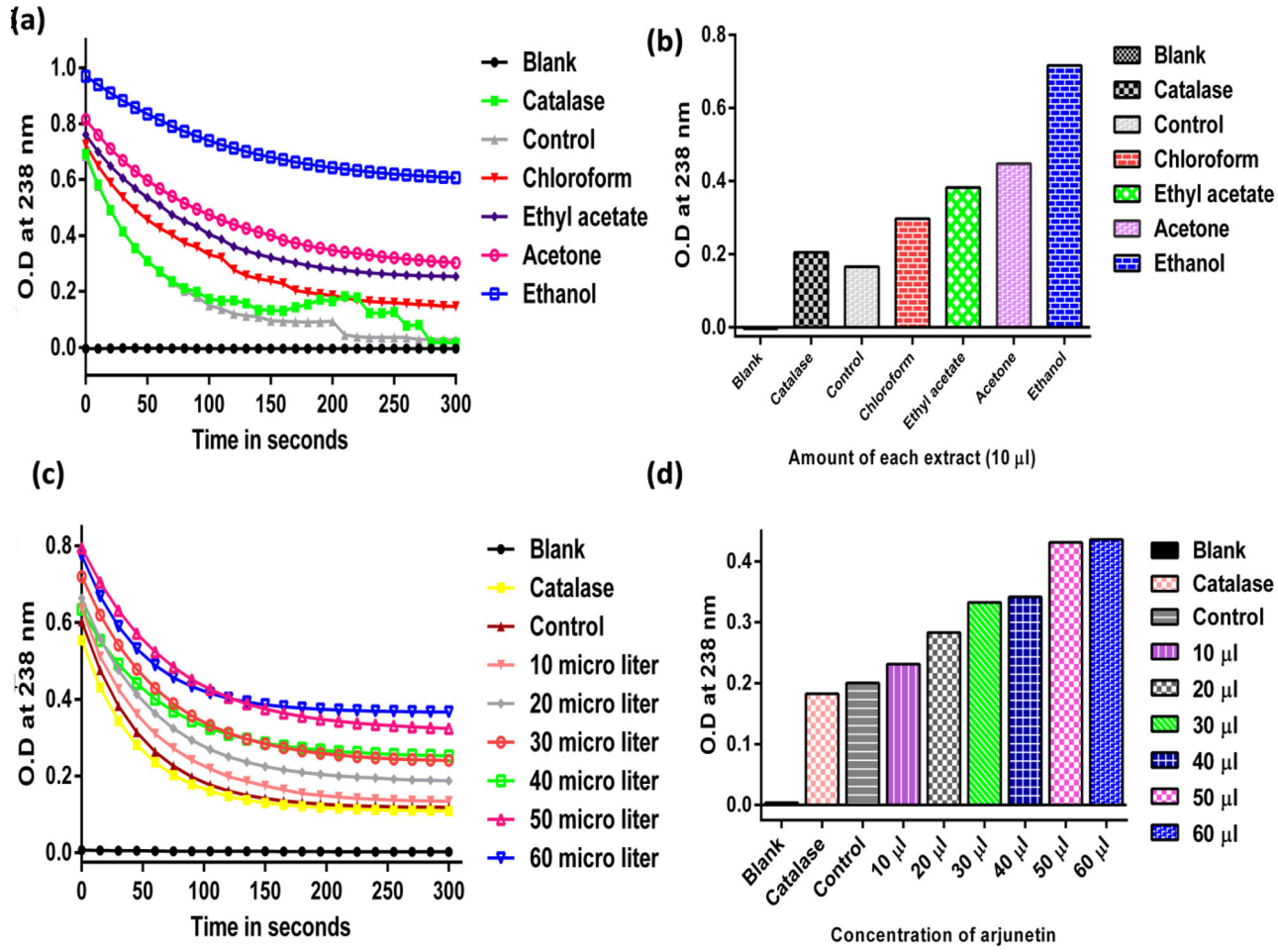

Figure 3. Effect of *T. arjuna* bark extracts on catalase activity. (a) Comparison of catalase activity with different *T. arjuna* bark extract. (b) Bar graph of the comparison of catalase activity with different *T. arjuna* bark extract. Effect of arjunetin from ethanol extract of *T. arjuna* bark on catalase activity. (c) Comparison of catalase activity with different amounts of arjunetin. (d) Bar graph of the comparison of catalase activity with different amounts of arjunetin.

(Gauthaman et al., 2005; Karthikeyan et al., 2003; Padma Sree et al., 2007).

The binding efficiency is attributed to the hydroxyl groups and ester glycoside present in arjunetin, which serve as hydrogen bond donors. The involvement of a positive charge on the carbon atom of the ester bond with the electronegative groups of amino acid residues like histidine also contributes towards efficient binding. Here it can be reasoned that at this concentration of arjunetin, it can also bind to other non-specific targets *in vivo* due to the presence of -OH groups.

Catalase is an antioxidant oligomeric enzyme (MW = 2,40,000) with four identical subunits arranged tetrahedrally. In eukaryotes, it plays an important role in protecting cells from oxidative damage due to ROS. However, in certain bacteria and viruses, catalase is present as an avirulent factor and is very important for the intracellular survival of the pathogen and disease progression. In this regard, compounds that bind to catalase and elicit enzyme inhibition which can act as efficient antimicrobial and antiviral agents. It is known that inhibitor 3-AT (an efficient inhibitor of catalase) binds with histidine residue (His75) near the heme group of catalase, forming a non-coplanar adduct (very close to Tyr358). Loss in the activity of catalase suggests the involvement of arjunetincation with histidine anion (*pKa* = 6.5) near tyrosine residue (Tyr358) of the active site. This information can be used in *in-silico* methods of drug development using arjunetin.

In the present study, physiological changes have been demonstrated by the inhibition of catalase by arjunetin. From the decay curves, as shown in Figure 3, it is inferred that the rate of H_2O_2 degradation is reduced by arjunetin, proving arjunetin to be a good catalase inhibitor and therefore has the potential to be studied for the development of an effective antibiotic.

Two main pathophysiologies of Covid-19 are its effect on the cardiovascular system and the development of adult respiratory distress syndrome (ARDS). Studies have shown that serum catalase activity increases in septic patients with ARDS (Leff et al., 1992). Considering the cardioprotective nature of *T. arjuna* and the ability to inhibit catalase, there is immense promise in this molecule for further research and use in the development of an effective cure against SARS-CoV-2.

3.4. Molecular docking studies

Since arjunetin showed a high inhibitory effect on catalase and its structure is similar to antiviral drugs, it was of our interest to study inhibition of SARS-CoV-2 proteases by

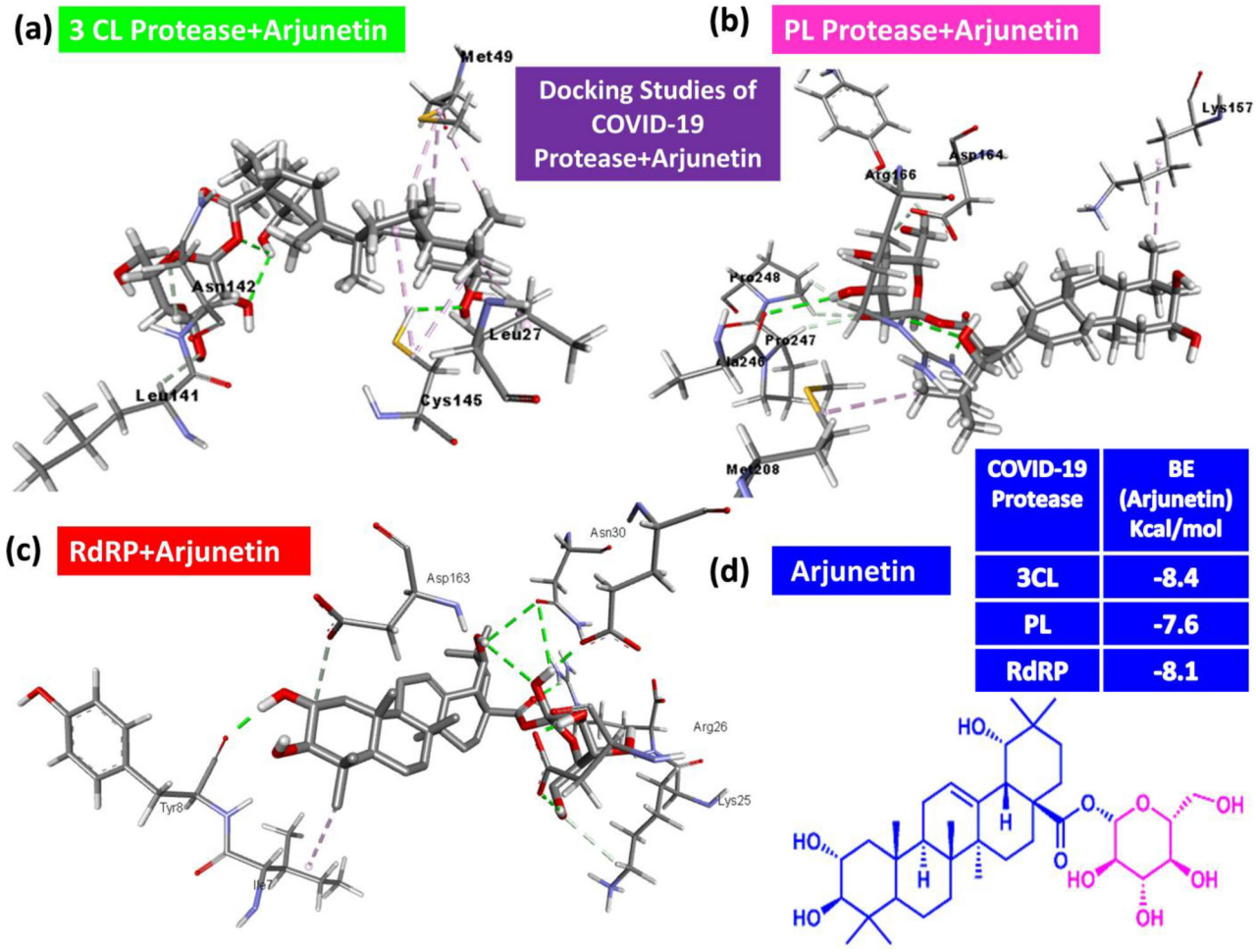

Figure 4. Molecular docking studies of SARS-CoV-2 protease with arjunetin (a) 3D interaction of 3CL + arjunetin, (b) 3D interaction of PL + arjunetin, (c) 3D interaction of RdRP with arjunetin, (d) Structure of arjunetin and binding energy values of SARS-CoV-2 protease with arjunetin.

arjunetin via molecular docking. Lopinavir and Remdesivir have been used as a control for our study (Manli et al., 2020; Stower et al., 2020; Maryam et al., 2021).

In this study, molecular docking of arjunetin was performed against SARS-CoV-2 3CL-protease, PL-protease, and RNA-polymerase. Lopinavir was used as a reference control for proteases. In the case of 3CL-protease, Arjunetin has better binding energy (−8.4 kcal/mol, K_i = 76 pM) compared to Lopinavir (−7.2 kcal/mol, K_i = 2.1 nM) (Figure 4). In the case of arjunetin, the interactions are predominantly hydrophobic due to the nonpolar part, contributed by LEU 141 and 27, whereas in the case of Lopinavir, it was hydrophilic. In the case of PL-protease, the Arjunetin binding score (−7.6 kcal/mol, K_i = 0.70 nM) is similar to Lopinavir (−7.74 kcal/mol, K_i = 0.53 nM) (Figure 5) and the binding score of Arjunetin towards SARs-CoV-2 RdRP polymerase was found to be −8.1 kcal/mol (K_i = 0.17 nM) (S-Table-1). Similarly, the binding score of SARs-CoV-2 RdRP with Remdesivir was found to be −7.6 kcal/mol (K_i = 0.70 nM) (Figure 6), thereby indicating that arjunetin might preferably inhibit 3CL-protease as compared to PL-protease and RNA polymerase and better binding energy values as compared to Remdesivir, Lopinavir (Table 1). These results, combined with the previously elucidated antioxidant and catalase inhibitory properties of arjunetin, make it a promising plant compound to be further evaluated against COVID-19.

3.5. Clustering analysis

Cluster analysis has been performed to determine structure populations from simulations (see computational details). The complete MD trajectory of each protease-inhibitor complex was clustered into 5-ensembles using a Hierarchical agglomerative approach (Shao et al., 2007). In Table 2, we have tabulated the percent contribution of each ensemble for all simulations. The representative structures of all significant contributing ensembles were superimposed to understand the conformational changes better. These ensembles primarily differed in the inhibitor molecule's orientation and positioning in different catalytic pockets. In Figures 7–12(a), we have depicted the superimposed structures of the highest populated ensembles, while in Figures 7–12(a-A), 7–12(a-B), and 11–12(a-C), separate figures of ensemble-1, -2, and -3 have been depicted with important hydrogen bonding interactions.

3.6. Molecular dynamics and analysis

We have calculated the root mean square deviation (RMSD) for each simulated system to explore the stability throughout the trajectory. The plots contain the RMSD fluctuations in (i) the receptor (red curves, protein), (ii) ligand RMSD with

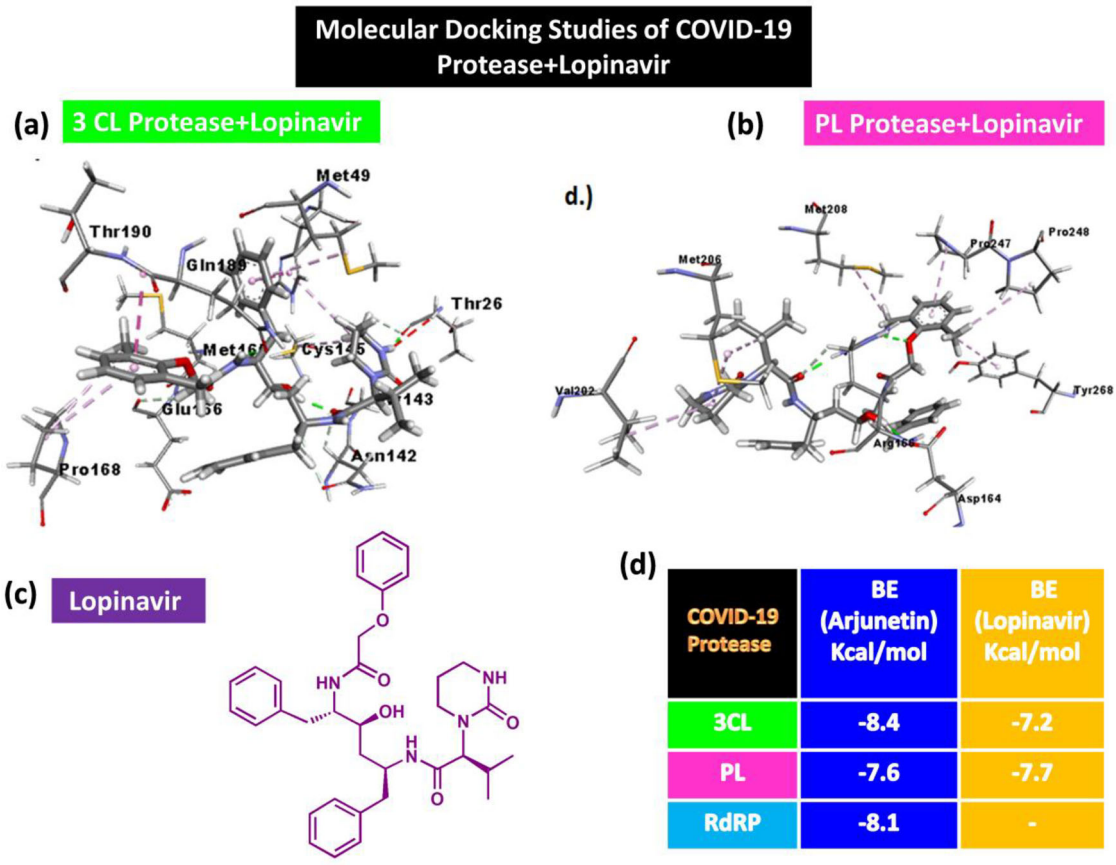

Figure 5. Molecular docking studies of SARS-CoV-2 protease with Lopinavir (a) 3D interaction of 3CL + Lopinavir, (b) 3D interaction of PL + Lopinavir, (c) Structure of Lopinavir, (d) Binding energy values of SARS-CoV-2 protease with Lopinavir.

respect to ligand (grey curves, Lig fit Lig), and (iii) ligand RMSD with respect to the receptor (green curves, Lig fit Prot). The Lig fit Lig RMSD is a direct measure of internal variations of the ligand atoms, and it is calculated by aligning the ligand to its first conformation. On the other hand, in Lig fit Prot, the receptor-ligand complex is aligned with the protein backbone in the first frame, and then the fluctuations in the ligand heavy atoms are measured. The Lig fit Prot describes the stability of the ligand to protein and its binding pocket.

In the case of 3 CL protease complexed with Arjunetin, the RMSD plot (Figure 7b) shows that the simulation is approaching a plateau within 2 ns with the protein and ligand RMSD values of 2.03 Å and 2.12 Å, respectively, indicating that 0–2 ns of the trajectory range should be sufficient one to reach the convergence. Furthermore, we have explored the ligand's stability relative to protein and found an average RMSD value of 2.85 Å after 140 ns of MD run. A sharp increase in the ligand's RMSD relative to protein is observed after 140 ns of simulation with a final average value of the deviation of 3.89 Å (Figure 7b). This sudden rise in ligand RMSD indicates that the ligand moves from one binding pocket to another during the simulation. Moreover, we have performed hydrogen-bond analysis (Figure 7c) throughout the trajectory, which indicates that a maximum number of the H-bonds (∼2–8) between 3 CL protease and Arjunetin has found between 0 ns to 140 ns, the number diminishes to zero for next 20 ns of trajectory, beyond which the average reaches to ∼0–3, suggesting a drastic change in the ligand positioning. Between 142 ns to 164 ns, no H-bonding interactions were found, indicating that the ligand has started to diffuse away from the binding pocket. This fact is in line with the sudden rise in the lig fit Prot RMSD plot after 140 ns depicted in Figure 7b. To validate the above observation, we have calculated the average interaction energies of arjunetin with the surrounding amino acid residues in the 3CL protease's binding pocket. For this, we have considered only those residues which are in close proximity to the ligand (within 6 Å). The average interaction energies are calculated by the summation of the van der Waals, electrostatic, polar solvation, and nonpolar solvation values for a particular residue (the internal energies were zero in all cases). The results indicate that Glu47 (−1.1 kcal/mol), Leu50 (−1.2 kcal/mol), Met165 (−0.9 kcal/mol), Leu167 (−1.0 kcal/mol), Gln189 (−2.2 kcal/mol), Thr190 (−2.1 kcal/mol), Gln192 (−2.3 kcal/mol) contribute to the most favourable interactions over all residues in the system while Ser46and Asn142are making the most unfavourable interactions (>0 kcal/mol) (Figure 7d). The principal component analysis reveals that the inhibitor is located between the Gln189 and Ser 46 residues, the former being highly stabilizing and the later destabilizing. As the simulation proceeds, Ser46 gradually moves away from arjunetin due to its unfavourable interactions with all other residues. It widens the path for the arjunetin to move, and under physiological conditions, the path becomes more solvent-exposed, facilitating the removal of the ligand from the

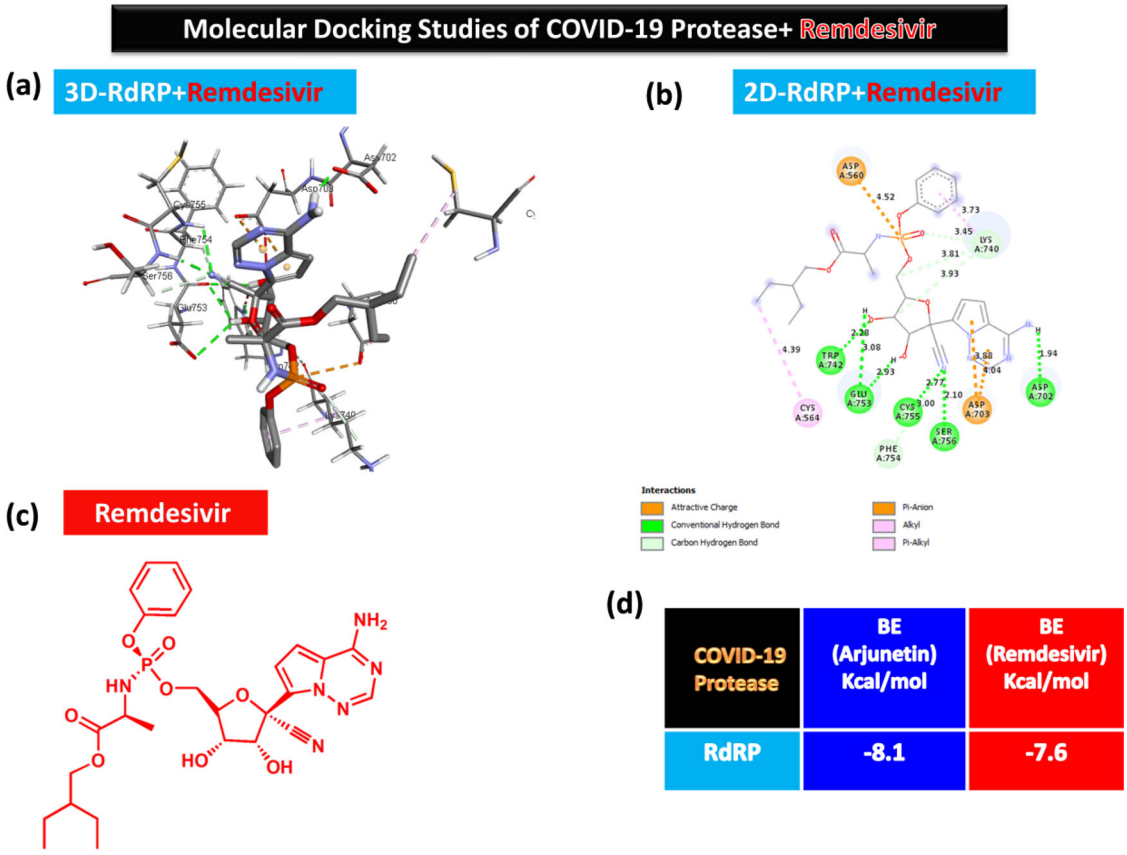

Figure 6. Molecular docking studies of SARS-CoV-2 protease RdRP with remdesivir. (a) 3D interaction of RdRP with remdesivir. (b) 2D interaction of RdRP with remdesivir. (c) Structure of remdesivir. (d) Binding energy values of SARS-CoV-2 protease RdRP with remdesivir.

Table 1. Key interaction of antivirals with amino acids in SARS-CoV-2 proteases; 3CL, PL, and RdRP with arjunetin, 3CL, and PL with Lopinavir and RdRP with Remdesivir.

Molecules	3CL-protease	PL-protease	RdRP
Arjunetin	Leu141, Leu27, Cys145, ASN12 and Met49	Pro248, Met208, Pro247, and Lys157	ARG26, Lys25, Asp160, Glu34, ASN30, Asp163, Tyr8, ILE 7
Lopinavir	Met 49, Pro168, ASN142, Cys145, Th190 and Thr 26	ASP164, Pro248, Met206, Val202, Tyr 260	–
Remdesivir	–	–	Asp560, Lys 740, Cys564, Trp742, Glu753, Cys755, Phe754, Ser756, Asp 703

Table 2. Percentage of occupancies of each ensemble out of 200 ns dynamics.

Protease-inhibitor complex	Ensemble 1	Ensemble 2	Ensemble 3	Ensemble 4	Ensemble 5
3CLprotease–Arjunetin	70.6%	19.3%	4.8%	2.7%	2.6%
PL protease–Arjunetin	47.8%	23.3%	17.7%	10.1%	1.0%
RdRP–Arjunetin	48.3%	35.2%	11.9%	3.9%	0.7 %
3CLprotease–Lopinavir	80.7%	9.0%	6.7%	3.4%	0.1%
PL protease–Lopinavir	50.7%	26.2%	10.7%	6.9%	5.5%
RdRP–Ramdesivir	42.4%	25.8%	20.3%	9.2%	2.3%

binding pocket. At the same time, Gln189, which has highly favourable interaction with the surroundings (−2.2 kcal/mol), was anchored to its position strictly and was not shifting to restrict the movement of the ligand. In the second binding pocket, significant stabilizing interaction is introduced by Trp218 (−0.2 kcal/mol), Asn277 (−0.2 kcal/mol), and Arg279 (−0.7 kcal/mol) residues responsible for locking the ligand in the binding site (Figure 7d). The distance RMSD plot (Figure 7e, red curve) between the two opposite residues, Ser 46 and Gln189, shows a continuous rise supporting the above fact. Moreover, we have compared the RMS deviation in the three connecting loops at the periphery of the first binding pocket, loop1 (residues 44–54), loop2 (residues175–200), and loop3 (residues130–147), and conclude that it is the outward movement of loop1 (containing Ser 46) responsible for the arjunetin removal (Figure 1e, loop1: green curve, loop2: pink curve, loop3: blue curve). In the previous study, Talarico and co-workers have described the conformational dynamics of the loops (residues 44–53 and 184–193), which are situated at the entrance of the 3CLp binding pocket (Grottesi et al., 2020). In the free protease, the Met49 and Arg188 groups are located at the entrance, and the inter-residue distance

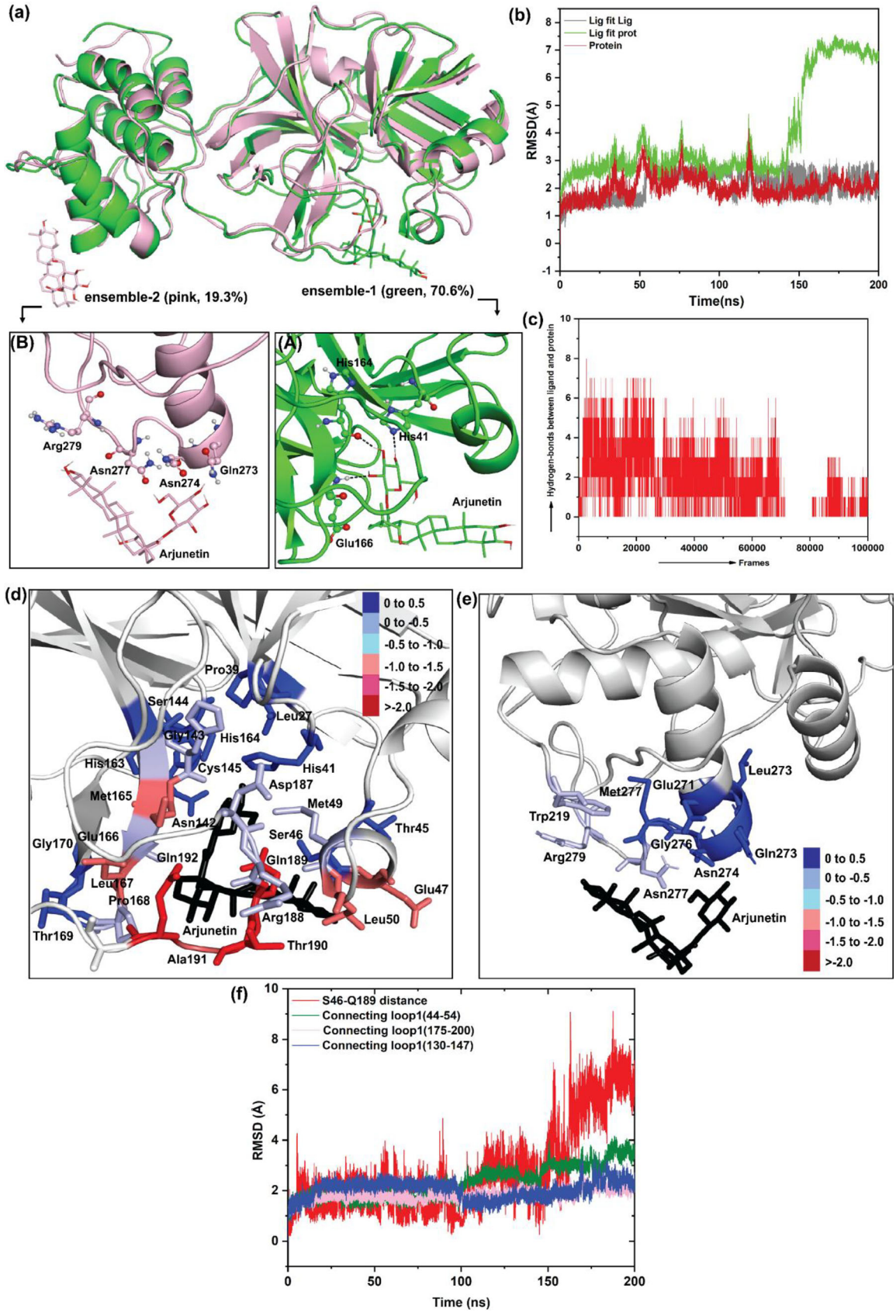

Figure 7. (a) Superimposition of most populated representative structures, ensemble 1 and 2 of 3 CL-protease-arjunetin complex with the neighbouring groups around the inhibitor ligand are showing for (A) ensemble 1 and (B) ensemble 2. Green and light pink colored cartoon representations are used for the ensemble 1 and ensemble 2 respectively. Important hydrogen bonds with the neighbouring residues have shown in black dashed lines. (b) Time dependent root mean square deviation (RMSD) graphs of arjunetin bound 3 CL-protease where RMSDs of the protein (brick red curve), Lig fit Lig (green curve), and Lig fit Prot (grey curve) are plotted against time (ns). Only heavy atoms of a ligand were considered. Deviations are calculated in Å unit. (c) Average of H-bonds throughout the trajectory of 3CLp-arjunetin complexes. (d) and (e) Energy per residue interaction plot of arjunetin, (d) in ensemble-1, and (e) in ensemble-2 obtained from MM-PBSA. Energies are in kcal/mol. (f) Distance RMSD plot for S46 and Q189 residues (red curve), time-dependent RMSDs for loop1 (44–54, deep green curve), loop2 (175–200, light pink curve), and loop3 (130–147, blue curve).

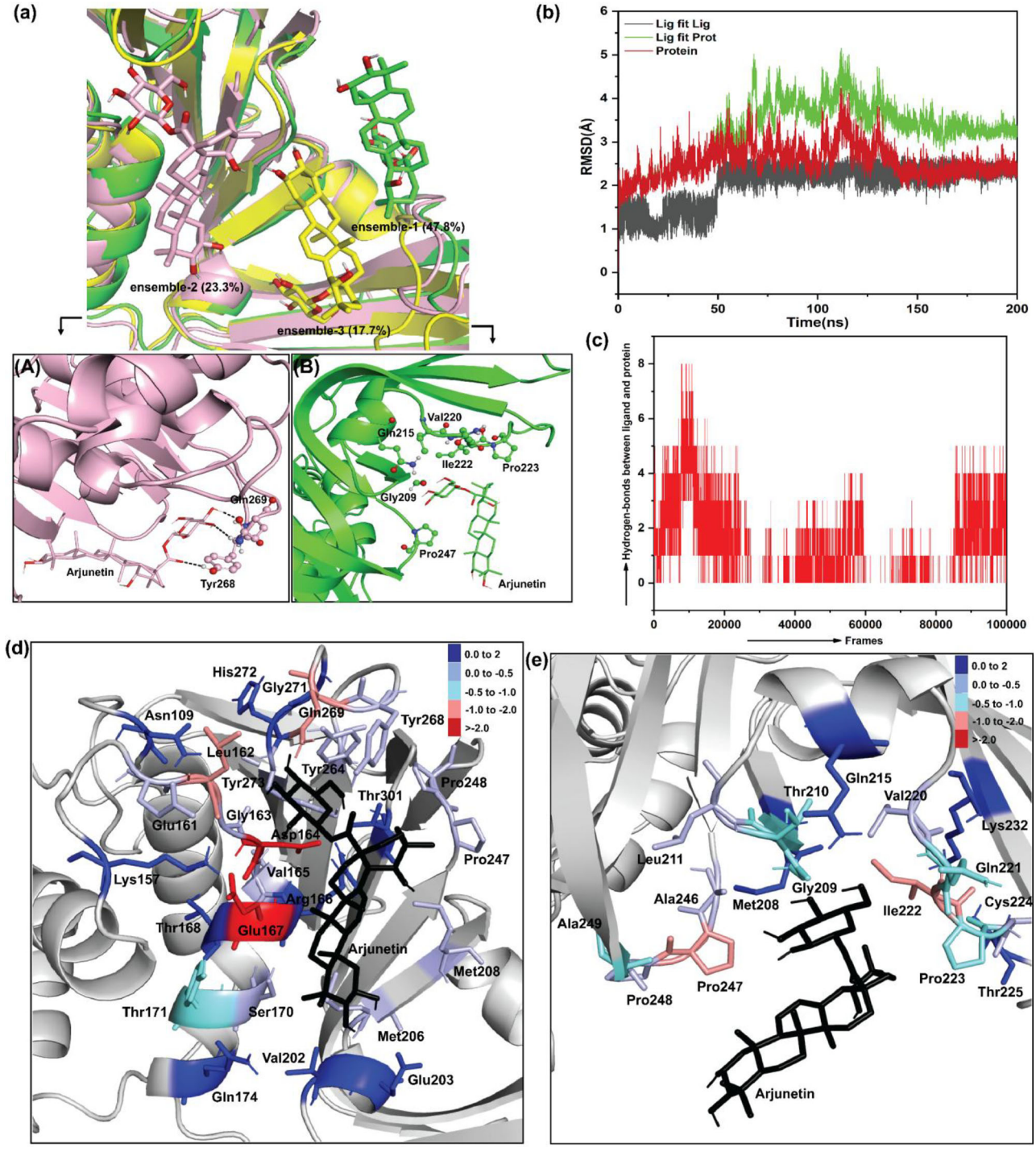

Figure 8. (a) Superimposition of most populated representative structures, ensemble 1, 2, and 2 of PL-protease-arjunetin complex with the neighbouring groups around the inhibitor ligand are showing for (A) ensemble 1 and (B) ensemble 2. Green, light pink, and yellow-colored cartoon representations are used for the ensemble 1, ensemble 2 and ensemble 3 respectively. Important hydrogen bonds with the neighbouring residues have shown in black dashed lines. (b) Time-dependent root mean square deviation (RMSD) graphs of arjunetin bound 3 CL-protease where RMSDs of the protein (brick red curve), Lig fit Lig (green curve), and Lig fit Prot (grey curve) are plotted against time (ns). Only heavy atoms of a ligand were considered. Deviations are calculated in Å unit. (c) Average of H-bonds throughout the trajectory of PL-protease-arjunetin complexes. (d) and (e) Energy per residue interaction plot of arjunetin (d) in ensemble-1 and (e) in ensemble-2 obtained from MM-PBSA. Energies are in kcal/mol.

increases during the simulation, leading to structural re-arrangements in the loops, resulting in the binding pocket region being more exposed to the bulk solvent. Our study is in agreement with the dynamic behaviour of the 3CL-protease observed earlier. We have estimated the free energy associated with the arjunetin binding in the different binding pockets of 3 CL protease using MM-PBSA script implemented in Amber 16and AmberTools packages. The calculated binding energy of the inhibitor in the first pocket is -21.7 ± 5.0 kcal/mol and in the second pocket is -3.7 ± 3.1 kcal/mol. Despite higher affinity in the first binding pocket, a high destabilizing polar solvation energy (27.4 ± 6.8 kcal/mol) is responsible for shifting the ligand to another binding pocket with comparatively less polar

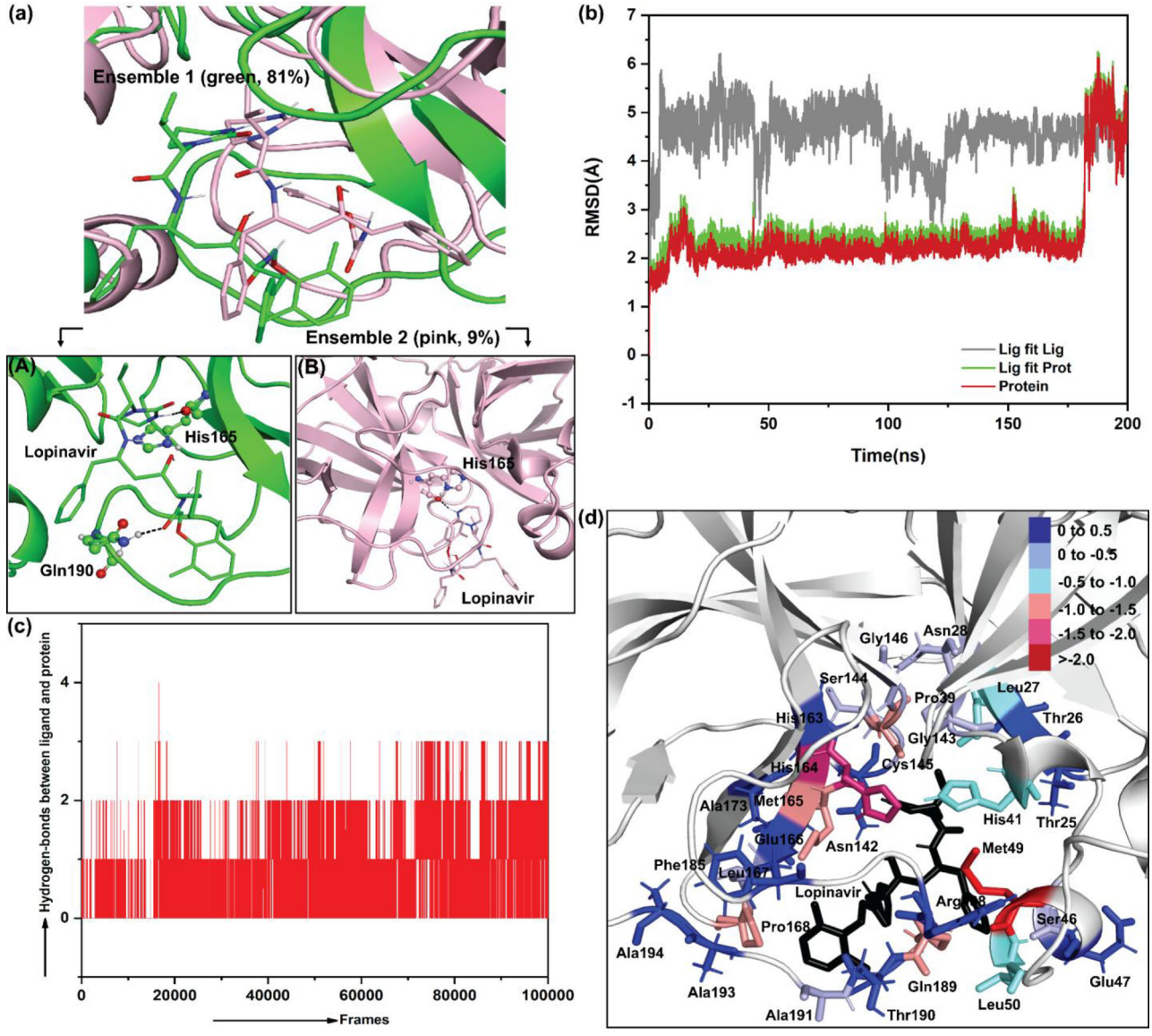

Figure 9. (a) Superimposition of most populated representative structures, ensemble 1 and 2 of 3 CL-protease-Lopinavir complexes with the neighbouring groups around the inhibitor ligand are showing for (A) ensemble-1 and (B) ensemble-2. Green and light pink colored cartoon representations are used for ensemble-1 and ensemble-2, respectively. Important hydrogen bonds with the neighbouring residues have shown in black dashed lines. (b) Time dependent root mean square deviation (RMSD) graphs of Lopinavir bound 3 CL-protease where RMSDs of the protein (brick red curve), Lig fit Lig (green curve), and Lig fit Prot (grey curve) are plotted against time (ns). Only heavy atoms of a ligand were considered. Deviations are calculated in Å unit. (c) Average of H-bonds throughout the trajectory of 3 CL-protease-Lopinavir complexes. (d) Energy per residue interaction plot of Lopinavir in the major contributing ensemble-1 obtained from MM-PBSA. Energies are in kcal/mol.

solvation energy (9.3 ± 3.1 kcal/mol). During the translational movement of the ligand, the entropy of the system is also increased by ~8 J K^{-1}, making the process spontaneous.

In contrast to 3 CL protease-arjunetin, the PL protease complexed with arjunetin reaches an equilibrium after the extended 160 ns of MD run and continued to remain stable, with an average RMSD value of 2.54 Å (Figure 8b). The ligand RMSD of rigid arjunetin reaches stability within 50 ns. Although the relative positioning of the ligand to protein is only partially stable, having the RMSD value in the range of 3–4 Å, the ligand remained bound to the same binding pocket. The PCA analysis confirms that the large fluctuation in the RMS value of protein and the Lig fit Prot between 70–140 ns is mainly due to the structural orientation of arjunetin during the simulation, and it is shifting towards the favourable interactions inside the same cavity. The maximum number of the H-bonds between the ligand (Arjunetin) and the receptor PL protease is found between 0 to 20 ns. After that, the number started to fall and again increases after 160 ns with the average reach to ~4 and remains stable. The 25,000 to 80,000 trajectory frames with the least number of interactions reflect the large fluctuations between 50

ns to 160 ns in the receptor structure and Lig fit Prot RMSD value (Figure 8c). Initially, the ligand is surrounded with the most unfavorable interactions (>0.05 kcal/mol) in one side exerted from Lys157 (1.5 kcal/mol), Arg166 (0.07 kcal/mol), Thr168 (0.2 kcal/mol), Gln174 (0.2 kcal/mol), Val202 (0.06 kcal/mol), Glu203 (0.1 kcal/mol), Thr301 (0.02 kcal/mol) residues (Figure 8d) enforce it for reorganization within the cavity and to move towards comparatively

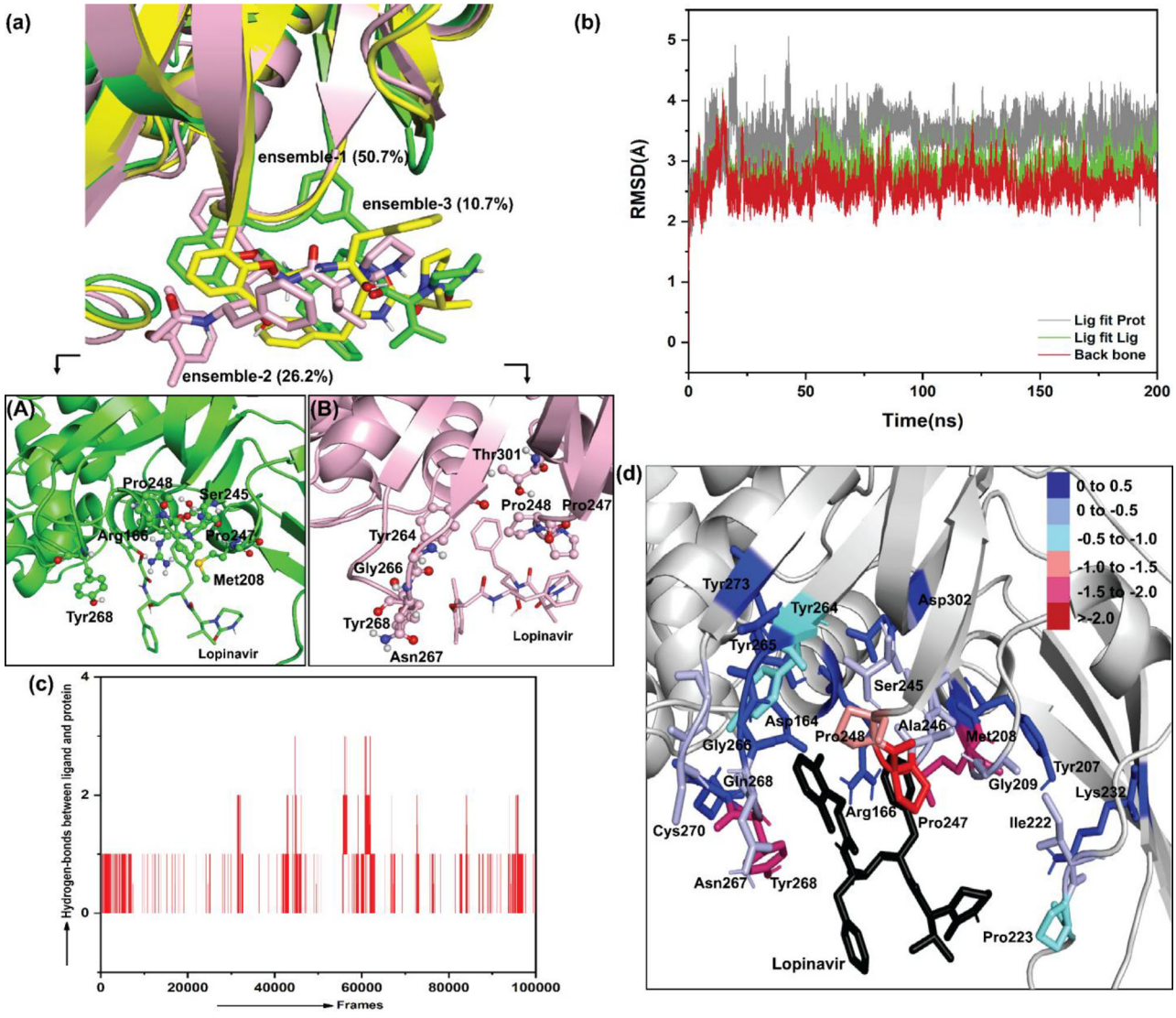

Figure 10. (a) Superimposition of most populated representative structures, ensemble-1 and ensemble-2 and ensemble-3 of PL-protease-Lopinavir complex with the neighbouring groups around the inhibitor ligand are showing for (A) ensemble-1 and (B) ensemble-2. Green and light pink colored cartoon representations are used for ensemble-1 and ensemble-2, respectively. Important hydrogen bonds with the neighbouring residues have shown in black dashed lines. (b) Time dependent root mean square deviation (RMSD) graphs of Lopinavir bound PL-protease where RMSDs of the receptor (brick red curve), Lig fit Lig (green curve), and Lig fit Prot (grey curve) are plotted against time (ns). Only heavy atoms of a ligand were considered. Deviations are calculated in Å unit. (c) Average of H-bonds throughout the trajectory of PL-protease-Lopinavir complexes. (d) Energy per residue interaction plot of Lopinavir in the major contributing ensemble-1 obtained from MM-PBSA. Energies are in kcal/mol.

more favorable interactions. Figure 8(a-B) represents ensemble 1. The interaction energies of the ligand (Figure 8d) in ensemble-1 shows that the ligand has moved to the side of the cavity with more stabilizing interactions around it, namely Gly209 (−0.8 kcal/mol), Gln221 (−0.8 kcal/mol), Ile222 (−1.1 kcal/mol), Pro223 (−0.8 kcal/mol), Pro247 (−1.4 kcal/mol), Pro248 (−0.4 kcal/mol) (Figure 8e). The final binding energy during the simulation is calculated to be −12.9 ± 3.6 kcal/mol towards 200 ns of MD run.

In the next set of protease-inhibitor systems, the 3CL protease complexed with Lopinavir, we observe a significant fluctuation from 7 ns to 20 ns in the protein RMSD (2.40 Å) which is in agreement with the previous studies on the same complex. In contrast to rigid arjunetin, where the ligand reaches an early equilibrium with low deviation, a large ligand RMSD (>4 Å) is observed for Lopinavir, which is still acceptable as the RMSD values are overestimated due to the rotation of symmetrical functional groups and the phenyl rings of the large molecule (Figure 9b). The PL protease-Lopinavir complex attains stability after 23 ns with a protein RMSD value of 2.61 Å (Figure 10b). Similar to 3CL protease-Lopinavir, the lig fit lig is also overestimated in this case. The average number of H-bonds between the receptor and ligand in the case of the 3CL protease-Lopinavir complex was ranging from 0 to 2, and this number increases to 3 as it approaches towards 200 ns, indicating a better stabilization of the ligand to the binding pocket (Figure 9c). This number is between 0 and 2 for PL protease-Lopinavir in most of the frames (Figure 10c). The MM-PBSA binding free energy of Lopinavir complexed with 3CL-protease is −27.5 ± 3.1 kcal/mol while that PL-protease is −15.9 ± 4.9 kcal/mol. The higher binding affinity of −5.8 kcal/mol of the Lopinavir towards 3CL-protease than that of arjunetin (before 140 ns, in the first binding pocket) is mainly due to the lowering of the polar

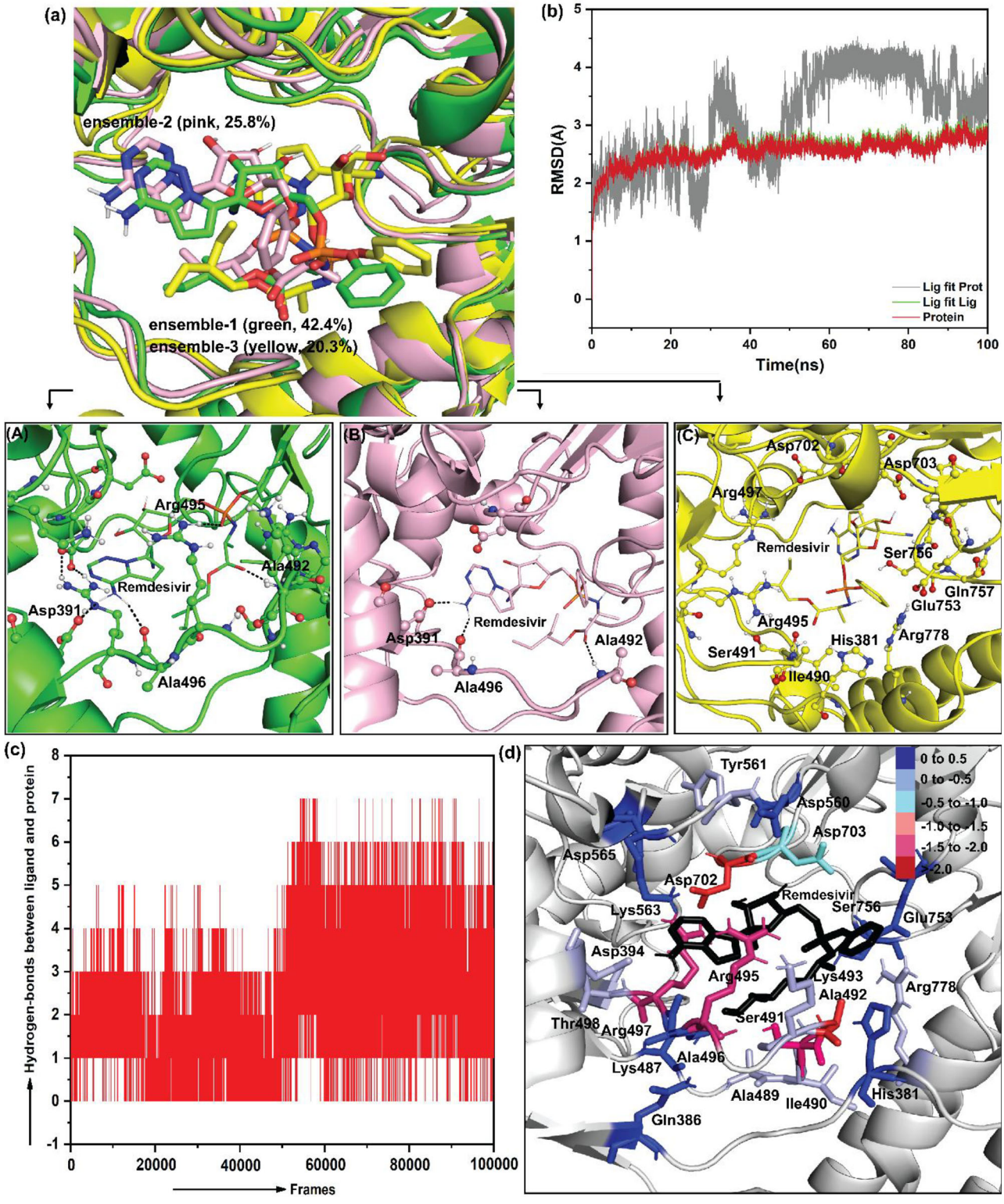

Figure 11. (a) Superimposition of most populated representative structures, ensemble-1, ensemble-2, and ensemble-3 of RNA-polymerase-Remdesivir complex with the neighbouring groups around the inhibitor ligand are showing for (A) ensemble-1, (B) ensemble-2, and (C) ensemble-3. Green, light pink, and yellow colored cartoon representations are used for the ensemble-1, -2, and -3, respectively. Important hydrogen bonds with the neighbouring residues have shown in black dashed lines. (b) Time dependent root mean square deviation (RMSD) graphs of Arjunetin bound RNA-Remdesivir where RMSDs of the protein (brick red curve), Lig fit Lig (green curve), and Lig fit Prot (grey curve) are plotted against time (ns). All atoms of a ligand were considered. Deviations are calculated in Å unit. (c) Average of H-bonds throughout the trajectory of RNA-polymerase-Remdesivir complexes. (d) Energy per residue interaction plot of arjunetin in the major contributing ensemble-1 obtained from MM-PBSA. Energies are in kcal/mol.

solvation energy by −11.8 kcal/mol for Lopinavir. Moreover, the stabilizing van der Waals interaction is 4.3 kJ/mol lower for arjunetin. Although the electrostatic interaction energy shifted by −10.1 kcal/mol for arjunetin, this stabilizing energy is more than compensated by the previously described van der Waals and polar solvation energies. PL-protease-arjunetin

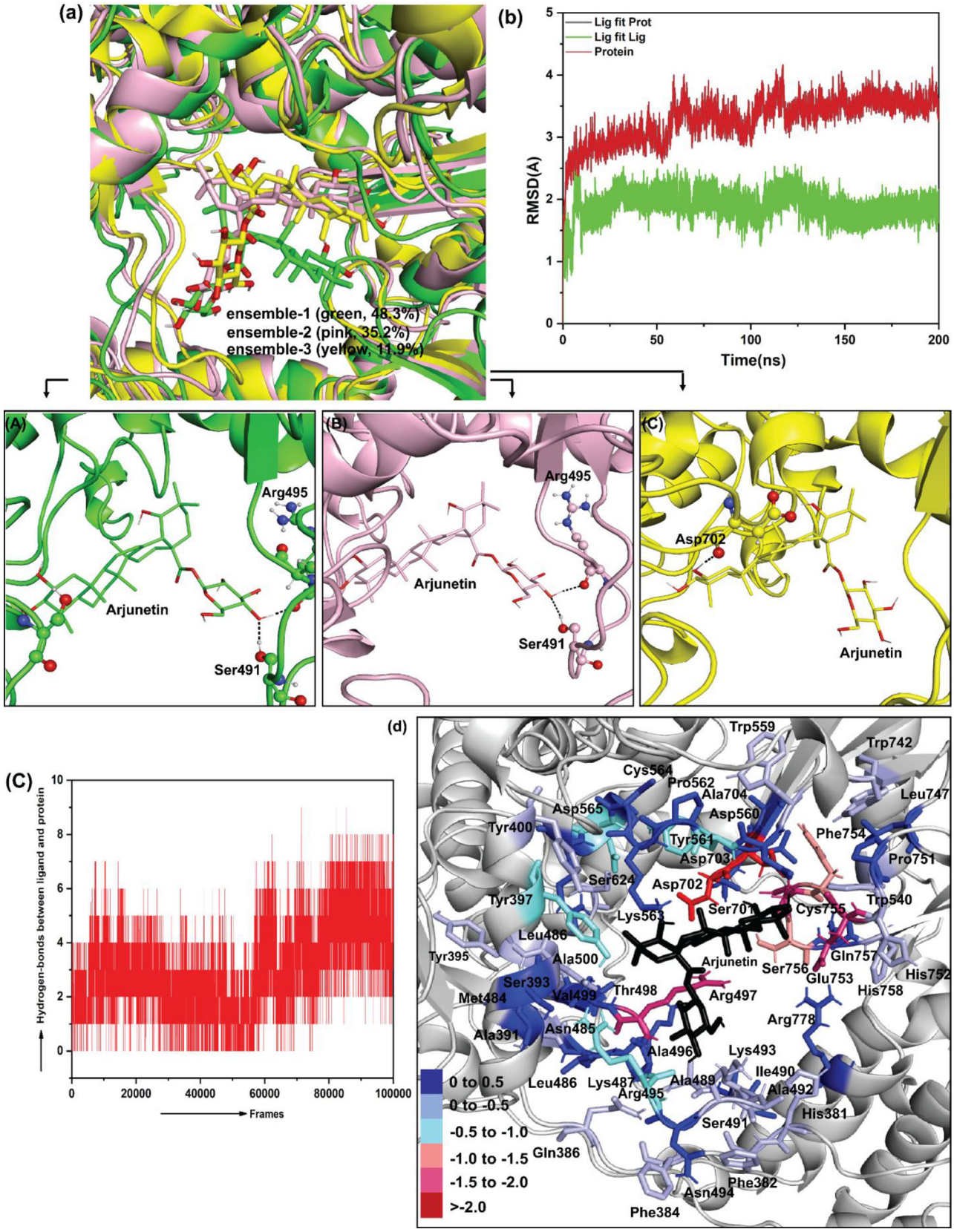

Figure 12. (a) Superimposition of most populated representative structures, ensemble-1, ensemble-2, and ensemble-3 of RNA-polymerase-Arjunetin complex with the neighbouring groups around the inhibitor ligand are showing for (A) ensemble-1, (B) ensemble-2, and (C) ensemble-3. Green, light pink, and yellow-colored cartoon representations are used for the ensemble-1, -2, and -3, respectively. Important hydrogen bonds with the neighbouring residues have shown in black dashed lines. (b) Time dependent root mean square deviation (RMSD) graphs of Arjunetin bound RNA-polymerase where RMSDs of the protein (brick red curve), Lig fit Lig (green curve), and Lig fit Prot (grey curve) are plotted against time (ns). All atoms of a ligand were considered. Deviations are calculated in Å unit. (c) Average of H-bonds throughout the trajectory of RNA-polymerase-Arjunetin complexes. (d) Energy per residue interaction plot of Arjunetin in the major contributing ensemble-1 obtained from MM-PBSA. Energies are in kcal/mol.

is found to be comparable with PL-protease-Lopinavir; in agreement with the experimental results, i.e. the binding free energy is 3 kcal/mol lower in the case of arjunetin. For 3CL protease-LopinavirLeu27 (−0.7 kcal/mol), His41 (−0.7 kcal/mol), Met49 (−3.0 kcal/mol), Cys145 (−1.2 kcal/mol), His164 (−1.8 kcal/mol), Met165 (−1.2 kcal/mol), Pro168 (−1.2 kcal/mol), Gln189 (−1.2 kcal/mol) groups contribute to the favorable interactions while Glu47 (0.1 kcal/mol), Asn142 (0.2 kcal/mol), Glu166 (0.3 kcal/mol), Arg188 (0.2 kcal/mol) contribute towards destabilization (Yogesh et al., 2020).

Several studies have been reported on the Remdesivir complexed with RNA-polymerase previously and proposed that the protein-inhibitor complex is relatively stable during the simulation, and the equilibration is achieved within 30 ns (Wakchaure et al., 2020). Therefore, to save the computational cost, we extend the simulation for the Remdesivir-bound RdRp to 100 ns. The protein and the Lig fit Lig RMSD of Remdesivir-bound RdRp are found to achieve equilibration within 40 ns and remain invariable during the entire simulation process. This is in agreement with the previous observations and provides confidence that a 100 ns simulation is enough to study the dynamics of the presently studied protein-inhibitor system. The Lig fit Prot graph shows a greater deviation and stabilizes during the last 10 ns of simulation, having an RMSD value of 2.8 Å. It reflects the fact that during the process, the ligand reorients inside the cavity get the maximum stabilization in terms of hydrogen bonding, van der Waals, electrostatic, polar, and nonpolar interactions. Figure 11(A)–(C) represents the highest populated ensembles during simulation A, where B represents the structures near 100 ns, C represents the starting frames, while A represents the intermediate frames. We can observe that initially, ensemble 3(C) with no stabilizing protein-ligand H-bonding interaction simulates towards ensemble 1(B), having the maximum number of stabilizing interactions (∼5). This fact is reflected in Figure 5(c), where the number of hydrogen bonds per frame between Remdesivir and protein is shown during the entire simulation. The maximum number of H-bond interactions (0 to 7) is observed after 50 ns which corresponds to the ensemble 1 and 2. The inhibitor's average binding energy inside the cavity is −7.6 ± 3.8 kcal/mol, which is in line with the predicted binding energy value of −7.6 kcal/mol. Figure 11(d) shows that the favorable interactions inside the cavity are coming from Ser491 (−1.9 kcal/mol), Ala492 (−2.2 kcal/mol), Arg495 (−1.8 kcal/mol), Arg497 (−1.9 kcal/mol), Asp702 (−2.1 kcal/mol) and Asp703 (−0.5 kcal/mol) residues while the most destabilizing interactions are exerted by the Asp560 (0.7 kcal/mol), Lys563 (0.6 kcal/mol), Asp565 (0.5 kcal/mol), Glu753(0.5 kcal/mol) residues.

In contrast to the Remdesivir-RNA-polymerase inhibitor-receptor system, the arjunetin complex RdRP reaches a late equilibration after 150 ns of the production run, having an average RMSD value of 3.28 Å during the simulation. Like the previous complexes, the rigid arjunetin molecule attains stability within 50 ns with a lower RMSD value of 1.89 Å. This indicates the arjunetin molecule to be highly rigid with a minimal internal deviation of the atoms. The almost superimposable protein and Lig fit Prot RMSD graphs indicate that the ligand is stable within the protein binding pocket; Only the receptor fluctuates during the simulation. The higher stability of the ligand inside the binding pocket reflects a greater value (∼3.13) of the average number of hydrogen bonds throughout the trajectory (Figure 12c). It shows that the number of H-bonding interactions between the receptor and the ligand increases gradually from 0 ns to 160 ns. The average reaches the maximum (4.9) after that and remains stable. The calculated binding energy of inhibitor arjunetin is −10.7 ± 4.4 kcal/mol, which is very close to the experimentally observed value of −7.8 kcal/mol. Figure 6(d) shows that inside the pocket, the inhibitor molecule is surrounded by the highly stabilizing Tyr397 (−0.7 kcal/mol), Arg495 (−0.9 kcal/mol), Arg497 (−1.9 kcal/mol), Tyr561 (−0.9 kcal/mol), Asp565 (−0.5 kcal/mol), Asp702 (−1.9 kcal/mol), Asp703 (−2.9 kcal/mol), Glu753 (−1.5 kcal/mol), Phe754 (−1.3 kcal/mol), Cys755 (−1.8 kcal/mol), Ser756 (−1.3 kcal/mol) residues and destabilizing Lys487 (0.6 kcal/mol), Lys563 (2.3 kcal/mol), Arg566 (2.2 kcal/mol), Ser701 (0.5 kcal/mol) residues. From the interaction energy value of the individual residues, we can conclude that several stabilizing interactions surround the inhibitor, restricting its movement during the simulation, which is also observable in the less deviation in the Lig fit Lig graph in Figure 12(b). The binding energy of arjunetin is higher than Remdesivir due to the greater stabilizing van der Waals (−21.4 ± 1.6 kcal/mol vs. −18.1 ± 1.7 kcal/mol, respectively) and electrostatic interactions (−30.3 ± 4.4 kcal/mol vs. −23.1 ± 3.7 kcal/mol, respectively). However, the destabilizing polar solvation energy for Arjunetin is higher (44.1 ± 4.0 kcal/mol) than Remdesivir (35.5 ± 3.3 kcal/mol). From the above comparative study, we can say that the binding affinity of Arjunetin (−10.7 kcal/mol) is higher than Remdesivir (−7.6 kcal/mol) in the binding cavity of RNA-polymerase. Although the former protein-inhibitor complex reaches a late equilibration (after 150 ns) compared to the RNA-polymerase-Remdesivir complex having an early stabilization, after equilibration, the inhibitor Arjunetin molecule is surrounded by several favorable interactions anchoring it strongly to the cavity. Therefore, Arjunetin is concluded to be a potent RdRp inhibitor.

We have extended the molecular dynamics simulation of CL-protease-arjunetin (300 ns), PL-protease-arjunetin (500 ns), and RNA-polymerase-arjunetin (350 ns) complexes and plotted time-dependent root mean square deviation (RMSD) graphs (see Figure 13). The RMSD plot with extended simulation time reveals a similar kind of behavior as observed for the 200 ns simulation. For CL-protease-arjunetin, we found a shifting of the binding region after 140 ns, and after 300 ns of extended MD run, the binding site remains constant, with the binding energy of 3.1 kcal/mol. The MM-PBSA calculated average binding energy of arjunetin in RNA-polymerase after 350 ns of simulation is −11.6 kcal/mol, which is −10.7 kcal/mol after 200 ns of MD run. Therefore, it is observed that after 200 ns there is no significant behavioral change has been found. The scenario is similar for the PL-protease-arjunetin complex (binding energy after 500 ns −15.7 kcal/mol).

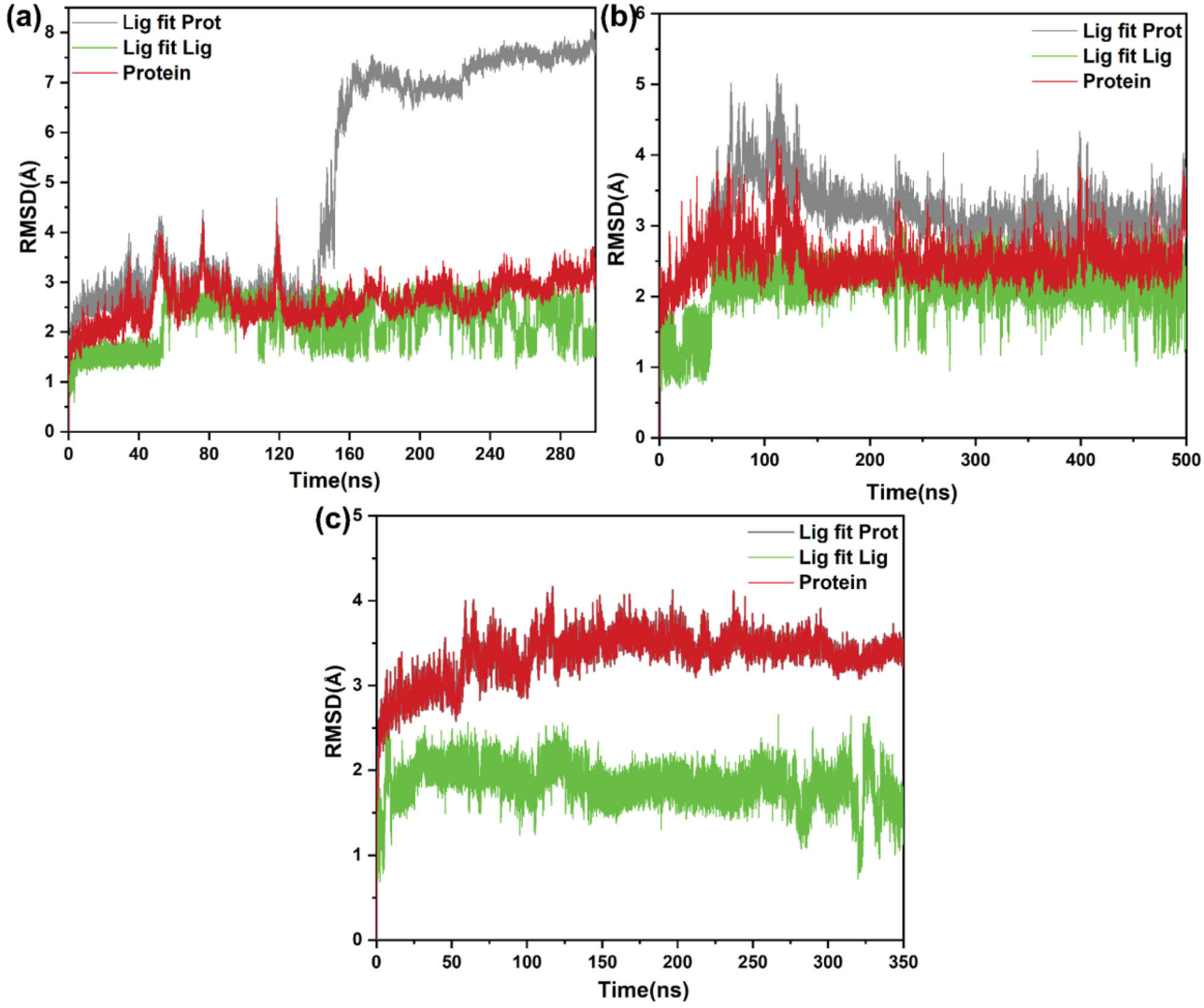

Figure 13. Time dependent RMSD graphs of (a) 300 ns of CL-protease-arjunetin, (b) 500 ns of PL-protease-arjunetin and (c) 350 ns of RNA-polymerase-arjunetin, where RMSDs of the protein (brick red curve), Lig fit Lig (green curve), and Lig fit Prot (grey curve) are plotted against time (ns). All atoms of a ligand were considered. Deviations are calculated in Å unit.

These observations provide confidence in our simulation results as well as simulation time.

Therefore, in the present study, we have screened a potent SARS-CoV-2-specific 3CL-protease (PDB entry 6lu7), PL-protease (PDB entry 6w9c), and RNA-polymerase (PDB:6M71) inhibitor arjunetin and compared the receptor-inhibitor stability as well as the binding mechanism of it with the previously reported widely accepted potential drugs Lopinavir and Remdesivir. Our MD study reveals that arjunetin is stable inside the binding pockets for a significant amount of time for several reasons (i) close proximity of several –OH groups facilitate strong H-bonding interaction with the residues, (ii) a rigid geometry offer stronger interaction at selected binding pockets and hinders rotational movements which tends to destabilize such as the one observed in Lopinavir, (iii) the –OH groups in arjunatin molecules are distributed in three different part of the molecule and this anchor the molecules inside the cavity via strong H-bonding offering larger stability, (iv) additionally several residues bearing charges found to have van der Waals and strong electrostatic interactions with the arjunatin molecule that binds it to the cavity favourably compared to others. From the above discussion, we can conclude that Arjunetin has a lot of potential as an inhibitor against three proteases of SARS-CoV-2 viz. 3CL, PL, and RdRP.

4. Conclusions

The present study was carried out to identify and evaluate active components in solvent extracts of *T. arjuna* bark samples, which is known for its cardioprotective and antimicrobial properties. Ethanolic extracts had a significantly higher free radical scavenging ability as compared to other extracts, indicating their antioxidant nature. Further, arjunetin purified from ethanolic bark extract showed dose dependent inhibition of catalase activity *in-vitro*. Molecular docking studies and Molecular dynamic simulation studies on arjunetin against three proteases of SARS-CoV-2 viz. 3CL, PL and RdRP demonstrated that arjunetin could bind more efficiently to the viral proteases as compared to known commercially available antivirals, thereby acting as an inhibitor. Therefore, in the present study, we have screened a potent SARS-CoV-

2-specific 3CL-protease (PDB entry 6lu7), PL-protease (PDB entry 6w9c) and RNA-polymerase (PDB: 6M71) inhibitor arjunetin and compared the receptor-inhibitor stability as well as the binding mechanism of it with the previously reported widely accepted potential drugs Lopinavir and Remdesivir. Based on these results, we can conclude that arjunetin is very much potential drug candidate against Covid-19.

Acknowledgments

The authors gratefully acknowledge Dr. Sreevidya Narasimhan, CDRI, Lucknow. The authors wish to thank the SAIF, Department of Chemistry, IIT Madras for EPR, FT-IR, NMR, ESIMS facility and Prof. Pradeepkumar Department of Chemistry, IIT Bombay, for helpful discussion.

Disclosure statement

The authors declare that they have no conflict of financial interest.

Funding

Prof. GSN acknowledges Industrial Consultancy and Sponsored Research, IIT Madras for providing exploratory research grant. Prof. GR would like to thank DST and SERB for funding (CRG/2018/000430; DST/SJF/CSA-03/2018-10; SB/SJF/2019-20/12).

ORCID

Kartik Mitra http://orcid.org/0000-0003-4891-1463
Mukesh Doble http://orcid.org/0000-0002-4335-0698
Gopalan Rajaraman http://orcid.org/0000-0001-6133-3026

References

Adevaiton, B. D. S., Dulce, H. S. S., Vanderlan, S. B., Luciana, A. S., Tome, M. S., & Oswaldo, B. (2009). Antioxidant properties of plant extract; an EPR and DFT comparative study of the reaction with DPPH, TEMPOL and spin trap DMPO. *Journal of the Brazilian Chemical Society*, *20*, 1483–1492.

Andersen, H. C. (1983). Rattle: A "velocity" version of the shake algorithm for molecular dynamics calculations. *Journal of Computational Physics*, *52* (1), 24–34. https://doi.org/10.1016/0021-9991(83)90014-1

Basu, M., Czinn, S. J., & Blanchard, T. G. (2004). Absence of catalase reduces long-term survival of *Helicobacter pylori* in macrophage phagosomes. *Helicobacter*, *9*(3), 211–216. https://doi.org/10.1111/j.1083-4389.2004.00226.x

Bayly, C. I., Cieplak, P., Cornell, W., & Kollman, P. A. (1993). A well-behaved electrostatic potential based method using charge restraints for deriving atomic charges: The RESP model. *The Journal of Physical Chemistry*, *97*(40), 10269–10280. https://doi.org/10.1021/j100142a004

Case, D. A., Cheatham, T. E., III, Darden, T., Gohlke, H., Luo, R., Merz, K. M., Jr., Onufriev, A., Simmerling, C., Wang, B., & Woods, R. J. (2005). The Amber biomolecular simulation programs. *Journal of Computational Chemistry*, *26*(16), 1668–1688.

Case, D. A., Darden, T. A., Cheatham, T. E., Simmerling, C. L., Wang, J., Duke, R. E., Luo, R., Crowley, M., Walker, R. C., & Zhang, W. (2008). Amber *10*.

Concetta, R., Carmen, F., Alessia, Z., Cristina, S., Gargano, F., Coscioni, E., Rossi, F., & Capuano, A. (2021). Cardiac events potentially associated to remdesivir: An analysis from the european spontaneous adverse event reporting system. *Pharmaceuticals*, *14*, 611. https://doi.org/10.3390/ph14070611

Cooper, E. L. (2005). Cam, eCAM, bioprospecting: The 21st century pyramid. *Evidence-Based Complementary and Alternative Medicine*, *2*(2), 125–127. https://doi.org/10.1093/ecam/neh094

Darden, T., Perera, L., Li, L., & Pedersen, L. (1999). New tricks for modelers from the crystallography toolkit the particle mesh Ewald algorithm and its use in nucleic acid simulations. *Structure*, *7*(3), R55–R60. https://doi.org/10.1016/S0969-2126(99)80033-1

Darden, T., York, D., & Pedersen, L. (1993). Particle mesh Ewald: An N·log (N) method for Ewald sums in large systems. *Journal of Chemical Physics*, *98*(12), 10089–10092. https://doi.org/10.1063/1.464397

Day, W. A., Jr., Sajecki, J. L., Pitts, T. M., & Joens, L. A. (2000). Role of catalase in *Campylobacter jejuni*intracellular survival. *Infection and Immunity*, *68*(11), 6337–6345. https://doi.org/10.1128/IAI.68.11.6337-6345.2000

DeLano, W. L. (2002). Pymol: An open-source molecular graphics tool. *CCP4 Newsletter on Protein Crystallography*, *40*, 82–92.

Dickson, C. J., Madej, B. D., Skjevik, Å. A., Betz, R. M., Teigen, K., Gould, I. R., & Walker, R. C. (2014). Lipid14: The amber lipid force field. *Journal of Chemical Theory and Computation*, *10*(2), 865–879. https://doi.org/10.1021/ct4010307

Dwivedi, S. (2007). *Terminalia arjuna* Wight &Arn.-a useful drug for cardiovascular disorders. *Journal of Ethnopharmacology*, *114*(2), 114–129. https://doi.org/10.1016/j.jep.2007.08.003

Dwivedi, S., & Chopra, D. (2014). Revisiting *Terminalia arjuna* - An ancient cardiovascular drug. *Journal of Traditional and Complementary Medicine*, *4*(4), 224–231. https://doi.org/10.4103/2225-4110.139103

Fox, T., & Kollman, P. A. (1998). Application of the RESP methodology in the parametrization of organic solvents. *The Journal of Physical Chemistry B*, *102*(41), 8070–8079. https://doi.org/10.1021/jp9717655

Frisch, M. J., Trucks, G. W., Schlegel, H. B., Scuseria, G. E., Robb, M. A., Cheeseman, J. R., Scalmani, G., Barone, V., Mennucci, B., Petersson, G. A., Nakatsuji, H., Caricato, M., Li, X., Hratchian, H. P., Izmaylov, A. F., Bloino, J., Zheng, G., Sonnenberg, J. L., Hada, M., … & Fox, D. J. (2009). *Gaussian 09, Revision D.01*.Gaussian, Inc., Wallingford, CT.

Gauthaman, K., Banerjee, S. K., Dinda, A. K., Ghosh, C. C., & Maulik, S. K. (2005). Terminalia arjuna (Roxb.) protects rabbit heart against ischemic-reperfusion injury: Role of antioxidant enzymes and heat shock protein. *Journal of Ethnopharmacology*, *96*(3), 403–409. https://doi.org/10.1016/j.jep.2004.08.040

Ghodke, P. P., Bommisetti, P., Deepak, T. N., & Pradeepkumar, P. I. (2019). Synthesis of N^2-deoxyguanosine modified DNAs and the studies on their translesion synthesis by the *E. coli* DNA polymerase IV. *The Journal of Organic Chemistry*, *84*(4), 1734–1747. https://doi.org/10.1021/acs.joc.8b02082

Grottesi, A., Beškер, N., Emerson, A., Manelfi, C., Beccari, A. R., Frigerio, F., Lindahl, E., Cerchia, C., & Talarico, C. (2020). Computational Studies of SARS-CoV-2 3CLpro: Insights from MD Simulations. *International Journal of Molecular Sciences*, *21*(15), 5346. https://doi.org/10.3390/ijms21155346

Honda, T., Murae, T., Tsuyuki, T., Takahashi, T., & Sawai, M. (1976). Chemical constituents from bark of *Terminalia arjuna*. *Bulletin of the Chemical Society of Japan*, *49*(11), 3213–3225. https://doi.org/10.1246/bcsj.49.3213

Hua, Y. C., Chun, C. C. L., & Ta, C. L. (2002). Anti-herpes simplex virus type 2 activity of casurinin from the bark of *Terminalia arjuna* Linn. *Antiviral Research*, *55*, 447–455.

Jain, S., Yadav, P. P., Gill, V., Vasudeva, N., & Singla, N. (2009). *Terminalia arjuna* a sacred medicinal plant, phytochemical and pharmacological profile. *Phytochemistry Reviews*, *8*(2), 491–502. https://doi.org/10.1007/s11101-009-9134-8

Justyna, P., Moriola, B. S., & Ivana, A. (2013). Study of the antioxidant properties of beers using electron paramagnetic resonance. *Food Chemistry*, *141*, 3042–3049.

Karthikeyan, B. R., Sarala Bai, K., Gauthaman, K., Sathish, K. S., & Niranjali, D. S. (2003). Cardioprotective effect of the alcoholic extract of *Terminalia arjuna* bark in an *in vivo* model of myocardial ischemic reperfusion injury. *Life Sciences*, *73*(21), 2727–2739. https://doi.org/10.1016/S0024-3205(03)00671-4

Kartik, M., Prasanth, G., Sushank, A., Gayathri, C., Basavaraju, R., & Mukesh, D. (2020). Dual inhibitors of SARS-CoV-2 proteases:

Pharmacophore and molecular dynamics based drug repositioning and phytochemical leads. *Journal of Biomolecular Structure and Dynamics*, 1-14.

Kim, C.-H. (2021). Anti–SARS-CoV-2 natural products as potentially therapeutic agents. *Frontiers in Pharmacology*, *12*, 590509. https://doi.org/10.3389/fphar.2021.590509

Larini, L., Mannella, R., & Leporini, D. L. (2007). Langevin stabilization of molecular-dynamics simulations of polymers by means of quasisymplectic algorithms. *The Journal of Chemical Physics*, *126*(10), 104101. https://doi.org/10.1063/1.2464095

Leff, J. A., Parsons, P. E., Day, C. E., Oppegard, M. A., Moore, E. E., Moore, F., & Repine, J. E. (1992). Increased hydrogen peroxide scavenging and catalase activity in serum from septic patients who subsequently develop the adult respiratory distress syndrome. *American Review of Respiratory Disease*, *146*(4), 985–989. https://doi.org/10.1164/ajrccm/146.4.985

Lukas, V. S., Maren, B., Mira, A., Leonie, S., Christiane, S. H., Eike, S., Daniel, T., Ulf, D., Carina, E., Oliver, W., & Adalbert, K. (2021). Glycyrrhizin effectively inhibits SARS-CoV-2 replication by inhibiting the viral main protease. *Viruses*, *13*, 609.

Maier, J. A., Martinez, C., Kasavajhala, K., Wickstrom, L., Hauser, K. E., & Simmerling, C. (2015). ff14SB: Improving the accuracy of protein side chain and backbone parameters from ff99SB. *Journal of Chemical Theory and Computation*, *11*(8), 3696–3713. https://doi.org/10.1021/acs.jctc.5b00255

Manca, C., Simon Paul, S., Barry, C. E., III, Freedman, V. H., & Kaplan, G. (1999). *Mycobacterium tuberculosis* catalase and peroxidase activitiesand resistance to oxidative killing in humanmonocytes*invitro*. *Infection and Immunity*, *67*(1), 74–79. https://doi.org/10.1128/IAI.67.1.74-79.1999

Manli, W., Cao, R., Leike, Z., Xinglou, Y., Jia, L., Mingyue, X., Zhengli, S., Zhihong, H., Wu, Z., & Gengfu, X. (2020). Remdesivir and chloroquine effectively inhibit the recently emerged novel coronavirus (2019-nCoV) in vitro. *Cell Research*, *30*(3), 269–271. https://doi.org/10.1038/s41422-020-0282-0

Mark, P., & Nilsson, L. (2001). Structure and dynamics of the TIP3P, SPC, and SPC/E water models at 298 K. *The Journal of Physical Chemistry A*, *105*(43), 9954–9960. https://doi.org/10.1021/jp003020w

Maryam, H., Wanqiu, C., Daliao, X., & Charles, W. (2021). Computational molecular docking and virtual screening revealed promising SARS-CoV-2 drugs. *Precision Clinical Medicine*, *18*(4), 1–16. https://doi.org/10.1093/pcmedi/pbab001

Miller, B. R., III, McGee, T. D., Jr., Swails, J. M., Homeyer, N., Gohlke, H., & Roitberg, A. E. (2012). MMPBSA.py: An efficient program for end-state free energy calculations. *Journal of Chemical Theory and Computation*, *8*(9), 3314–3321. https://doi.org/10.1021/ct300418h

Moure, A., Franco, D., Sineiro, J., Domı́nguez, H., Núñez, M. J., & Lema, J. M. (2001). Antioxidant activity of extracts from *Gevuinaavellana* and *Rosa rubiginosa* defatted seeds. *Food Research International*, *34*(2–3), 103–109. https://doi.org/10.1016/S0963-9969(00)00136-8

Newcomb, W. W., & Brown, J. C. (2012). Internal catalase protects Herpes Simplex virus from inactivation by hydrogen peroxide. *Journal of Virology*, *86*(21), 11931–11934. https://doi.org/10.1128/JVI.01349-12

Ningjian, L., & David, D. K. (2014). Antioxidant property of coffee components: Assessment of methods that define mechanisms of action. *Molecules*, *19*, 19181–19208.

Novel Coronavirus (2019-nCoV) situation reports - 116, 15 May. (2020). https://www.who.int/emergencies/diseases/novelcoronavirus-2019/situation-reports.

Oleg, T., & Olson, A. J. (2010). Auto Dock Vina: Improving the speed and accuracy of docking with a new scoring function, efficient optimization, and multithreading. *Journal of Computational Chemistry*, *31*(2), 455–461.

Orhan, D. D., Yeşilada, F. E. E., Tsuchiya, K., Takaishi, Y., & Kawazoe, K. (2007). Antioxidant activity of two flavonol glycosides from *Cirsiumhypoleucum* DC through bioassay-guided fractionation. *Turkish Journal of Pharmaceutical Sciences*, *41*, 1–14.

Padma Sree, T. N., Krishna Kumar, S., Senthilkumar, A., Aradhyam, G. K., and Gummadi, S. N. P. (2007). *In vitro* effect of *Terminalia arjuna* bark extract on antioxidant enzyme catalase. *Journal of Pharmacology and Toxicology*, *2*(8), 698–708. https://doi.org/10.3923/jpt.2007.698.708

Patil, U. H., & Gaikwad, D. K. (2011). Phytochemical evaluation and bactericidal potential of *Terminalia arjuna* stem bark. *International Journal of Pharmaceutical Sciences and Research*, *2*, 614–619.

Pawar, R. S., & Bhutani, K. K. (2005). Effect of oleanane triterpenoids from *Terminalia arjuna*-a cardioprotective drug on the process of respiratory oxyburst. *Phytomedicine*, *12*(5), 391–393. https://doi.org/10.1016/j.phymed.2003.11.007

Pearlman, D. A., Case, D. A., Caldwell, J. W., Ross, W. S., Cheatham, T. E., III, DeBolt, S., Ferguson, D., Seibel, G., & Kollman, P. (1995). AMBER, a package of computer programs for applying molecular mechanics, normal mode analysis, molecular dynamics and free energy calculations to simulate the structural and energetic properties of molecules. *Computer Physics Communications*, *91*(1–3), 1–41. https://doi.org/10.1016/0010-4655(95)00041-D

Petrova, S. S., & Solov'ev, A. D. (1997). The origin of the method of steepest descent. *Historia Mathematica*, *24*(4), 361–375. https://doi.org/10.1006/hmat.1996.2146

Pettersen, E. F., Goddard, T. D., Huang, C. C., Couch, G. S., Greenblatt, D. M., Meng, E. C., & Ferrin, T. E. (2004). UCSF Chimera-a visualization system for exploratory research and analysis. *Journal of Computational Chemistry*, *25*(13), 1605–1612. https://doi.org/10.1002/jcc.20084

Priyadarshinee, S. P. P., Bommisetti, P., Diveshkumar, K. V., & Pradeepkumar, P. I. (2016). Benzothiazole hydrazones of furylbenzamides preferentially stabilize *c-MYC* and *c-KIT1* promoter G-quadruplex DNAs. *Organic & Biomolecular Chemistry*, *14*, 5779–5793.

Roe, D. R., & Cheatham, T. E. (2013). III, TE PTRAJ and CPPTRAJ: Software for processing and analysis of molecular dynamics trajectory data. *Journal of Chemical Theory and Computation*, *9*(7), 3084–3095. https://doi.org/10.1021/ct400341p

Roth, S., & Droge, W. (1987). Regulation of T cell growth factor (TCGF) production by hydrogen peroxide. *Cellular Immunology*, *108*(2), 417–424. https://doi.org/10.1016/0008-8749(87)90224-3

Salomon-Ferrer, R., Case, D. A., & Walker, R. C. (2013a). An overview of the Amber biomolecular simulation package. *Wiley Interdisciplinary Reviews: Computational Molecular Science*, *3*(2), 198–210. https://doi.org/10.1002/wcms.1121

Salomon-Ferrer, R., Götz, A. W., Poole, D., Le Grand, S., & Walker, R. C. (2013b). Routine microsecond molecular dynamics simulations with AMBER on GPUs. 2. Explicit solvent particle mesh Ewald. *Journal of Chemical Theory and Computation*, *9*(9), 3878–3888. https://doi.org/10.1021/ct400314y

Schreck, R., Rieber, P., & Baeuerle, P. A. (1991). Reactive oxygen intermediates as apparently widely used messengers in the activation of the NF-kappaB transcription factor and HIV-1. *The EMBO Journal*, *10*(8), 2247–2258.

Seong, W. C., Jin, S., Shin, S., Park, J., Eunhye, J., Yun, G. P., Jiho, L., Sung, J. K., Hun, Jun, P., Jung, H. L., Sung, M. P., Sung, H. M., Kiwon, B., & Yun, Y. G. (2020). Antiviral activity and safety of remdesivir against SARS-CoV-2 infection in human pluripotent stem cell-derived cardiomyocytes. *Antiviral Research*, *184*, 104955. https://doi.org/10.1016/j.antiviral.2020.104955

Shao, J., Tanner, S. W., Thompson, N., & Cheatham, T. E. (2007). Clustering molecular dynamics trajectories: 1. Characterizing the performance of different clustering algorithms. *Journal of Chemical Theory and Computation*, *3*(6), 2312–2334. https://doi.org/10.1021/ct700119m

Shewchuk, J. R. (1994). An introduction to the conjugate gradient method without the agonizing pain.

Sinosh, S., Dharshini, G., Aditi, G. M., Akshay, U., & Vidya, N. (2021). Structural insights on the interaction potential of natural leads against major protein targets of SARS-CoV-2: Molecular modelling, docking and dynamic simulation studies. *Computers in Biology and Medicine*, *132*, 104325.

Sinosh, S., Dharshini, G., Shweta, C., Priya, K., Akshay, U., Aditi, G. M., & Vidya, N. (2020). Structural and molecular basis of the interaction mechanism of selected drugs towards multiple targets of SARS-CoV-2 by molecular docking and dynamic simulation studies-deciphering

the scope of repurposed drugs. *Computers in Biology and Medicine*, *126*, 104054.

Stower, H. (2020). Lopinavir-titonavir in severe COVID-19. *Nature Medicine*, *26*, 465.

Sumitra, M., Manikandan, P., Kumar, D. A., Arutselvan, N., Balakrishna, K., Manohar, B. M., & Puvanakrishnan, R. (2001). Experimental myocardial necrosis in rats: Role of arjunolic acid on platelet aggregation, coagulation and antioxidant status. *Molecular and Cellular Biochemistry*, *224*(1-2), 135–142.

Sunyana, J., Prem, P.Y., Vikrant, G., Neeru, V., Neelam, S. (2009). Terminalia arjuna a sacred medicinal plant, phytochemical and pharmacological profile. Phytochemistry Reviews, 8, 491–502.

Tripathi, V. K., & Singh, B. (1996). *Terminalia arjuna* - its present status (a review). *Oriental Journal of Chemistry*, *12*, 1–16.

Wakchaure, P. D., Ghosh, S., & Ganguly, B. (2020). Revealing the inhibition mechanism of RNA-dependent RNA polymerase (RdRp) of SARS-CoV-2 by remdesivir and nucleotide analogues: A molecular dynamics simulation study. *The Journal of Physical Chemistry B*, *124*(47), 10641–10652. https://doi.org/10.1021/acs.jpcb.0c06747

Wang, J., Wolf, R. M., Caldwell, J. W., Kollman, P. A., & Case, D. A. (2004). Development and testing of a general amber force field. *Journal of Computational Chemistry*, *25*(9), 1157–1174. https://doi.org/10.1002/jcc.20035

WHO. (2012). *The evolving threat of antimicrobial resistance: Options for action*. WHO.

Wu, F., Zhao, S., Yu, B., Chen, Y.-M., Wang, W., Song, Z.-G., Hu, Y., Tao, Z.-W., Tian, J.-H., Pei, Y.-Y., Yuan, M.-L., Zhang, Y.-L., Dai, F.-H., Liu, Y., Wang, Q.-M., Zheng, J.-J., Xu, L., Holmes, E. C., & Zhang, Y.-Z. (2020). new coronavirus associated with human respiratory disease in China. *Nature*, *579*(7798), 265–269. https://doi.org/10.1038/s41586-020-2008-3

Xian, Y., Zhang, J., Bian, Z., Zhou, H., Zhang, Z., Lin, Z., & Xu, H. (2020). Bioactive natural compounds against human coronaviruses: A review and perspective. *Acta Pharmaceutica Sinica B*, *10*(7), 1163–1174. https://doi.org/10.1016/j.apsb.2020.06.002

Yogesh, K., Harvijay, S., & Chirag, N. P. (2020). *In silico* prediction of potential inhibitors for the main protease of SARS-CoV-2 using molecular docking and dynamics simulation based drug-repurposing. *Journal of Infection and Public Health*, *13*(9), 1210–1223.

Yu, W.-L., Toh, H. S., Liao, C.-T., & Chang, W.-T. (2021). A double-edged sword-cardiovascular concerns of potential anti-COVID-19 drugs. *Cardiovascular Drugs and Therapy*, *35*(2), 205–214. https://doi.org/10.1007/s10557-020-07024-7

Zhaoyan, Z., Yuchen, X., Lingqing, X., Ye, L., Guanmin, J., Wang, W., Li, B., Tianchuan, Z., Qingqin, T., Lantian, T., Haibo, Z., Xi, H., & Hong, S. (2021). Glycyrrhizic acid nanoparticles as antiviral and anti-inflammatory agents for COVID-19 treatment. *ACS Applied Materials & Interfaces*, *2021*(13), 18.

Zivkovic, J., Zekovic, Z., Music, I., Tumbas, V., Cvetkovic, D., & Spasojevic, I. (2009). Antioxidant properties of phenolics in *Castanea sativa* Mill. extracts. *Food Technology and Biotechnology*, *47*, 421–427.